

This is a repository copy of A luminous red optical flare and hard x-ray emission in the tidal disruption event AT 2024kmq.

White Rose Research Online URL for this paper: https://eprints.whiterose.ac.uk/id/eprint/233047/

Version: Published Version

Article:

Ho, A.Y.Q. orcid.org/0000-0002-9017-3567, Yao, Y. orcid.org/0000-0001-6747-8509, Matsumoto, T. orcid.org/0000-0002-3809-0000 et al. (30 more authors) (2025) A luminous red optical flare and hard x-ray emission in the tidal disruption event AT 2024kmq. The Astrophysical Journal, 989. 54. ISSN: 0004-637X

https://doi.org/10.3847/1538-4357/ade8f2

Reuse

This article is distributed under the terms of the Creative Commons Attribution (CC BY) licence. This licence allows you to distribute, remix, tweak, and build upon the work, even commercially, as long as you credit the authors for the original work. More information and the full terms of the licence here: https://creativecommons.org/licenses/

Takedown

If you consider content in White Rose Research Online to be in breach of UK law, please notify us by emailing eprints@whiterose.ac.uk including the URL of the record and the reason for the withdrawal request.



OPEN ACCESS



A Luminous Red Optical Flare and Hard X-Ray Emission in the Tidal Disruption Event AT 2024kmq

```
Anna Y. Q. Ho<sup>1</sup>, Yuhan Yao<sup>2,3</sup>, Tatsuya Matsumoto<sup>4,5</sup>, Genevieve Schroeder<sup>1</sup>, Eric R. Coughlin<sup>6</sup>, Daniel A. Perley<sup>7</sup>, Igor Andreoni<sup>8</sup>, Eric C. Bellm<sup>9</sup>, Tracy X. Chen<sup>10</sup>, Ryan Chornock<sup>3</sup>, Sofia Covarrubias<sup>11</sup>, Kaustav Das<sup>11</sup>, Christoffer Fremling<sup>11,12</sup>, Marat Gilfanov<sup>13</sup>, K. R. Hinds<sup>7</sup>, Dan Jarvis<sup>14</sup>, Mansi M. Kasliwal<sup>11</sup>, Chang Liu<sup>15,16</sup>, Joseph D. Lyman<sup>17</sup>, Frank J. Masci<sup>10</sup>, Thomas A. Prince<sup>11</sup>, Vikram Ravi<sup>11</sup>, R. Michael Rich<sup>18</sup>,
                           Reed Riddle<sup>12</sup>, Cassie Sevilla<sup>1</sup>, Roger Smith<sup>12</sup>, Jesper Sollerman<sup>19</sup>, Jean J. Somalwar<sup>11</sup>
             Gokul P. Srinivasaragavan <sup>20,21,22</sup>, Rashid Sunyaev <sup>13</sup>, Jada L. Vail <sup>1</sup>, Jacob L. Wise <sup>7</sup>, and Sol Bin Yun <sup>11</sup>, Department of Astronomy, Cornell University, Ithaca, NY 14853, USA
                                                      <sup>2</sup> Miller Institute for Basic Research in Science, 468 Donner Lab, Berkeley, CA 94720, USA

    Department of Astronomy, University of California, Berkeley, 501 Campbell Hall, Berkeley, CA 94720, USA
    Department of Astronomy, University of California, Berkeley, 501 Campbell Hall, Berkeley, CA 94720, USA
    Department of Astronomy, Kyoto University, Kitashirakawa-Oiwake-cho, Sakyo-ku, Kyoto, 606-8502, Japan
    Hakubi Center, Kyoto University, Yoshida-honmachi, Sakyo-ku, Kyoto, 606-8501, Japan
    Department of Physics, Syracuse University, Syracuse, NY 13210, USA

            Astrophysics Research Institute, Liverpool John Moores University, IC2, Liverpool Science Park, 146 Brownlow Hill, Liverpool L3 5RF, UK

8 University of North Carolina at Chapel Hill, 120 E. Cameron Ave., Chapel Hill, NC 27514, USA
                                <sup>9</sup> DIRAC Institute, Department of Astronomy, University of Washington, 3910 15th Ave. NE, Seattle, WA 98195, USA
<sup>10</sup> IPAC, California Institute of Technology, 1200 E. California Blvd., Pasadena, CA 91125, USA
                                   Division of Physics, Mathematics and Astronomy, California Institute of Technology, Pasadena, CA 91125, USA

12 Caltach Osteol Observatoriae California Institute of Technology Pasadena, CA 91125, USA
                                                        Caltech Optical Observatories, California Institute of Technology, Pasadena, CA 91125, USA
                                                    13 Max-Planck-Institut für Astrophysik, Karl-Schwarzschild-Str. 1, D-85741 Garching, Germany
                         <sup>14</sup> Astrophysics Research Cluster, School of Mathematical and Physical Sciences, University of Sheffield, Sheffield S3 7RH, UK
                                         Department of Physics and Astronomy, Northwestern University, 2145 Sheridan Rd., Evanston, IL 60208, USA
   <sup>16</sup> Center for Interdisciplinary Exploration and Research in Astrophysics (CIERA), Northwestern University, 1800 Sherman Ave., Evanston, IL 60201, USA
                                 17 Department of Physics, University of Warwick, Coventry CV4 7AL, UK
18 Department of Physics and Astronomy, UCLA, 430 Portola Plaza, Box 951547, Los Angeles, CA 90095-1547, USA
                                   <sup>19</sup> Department of Astronomy, The Oskar Klein Centre, Stockholm University, AlbaNova, 10691 Stockholm, Sweden
<sup>20</sup> Department of Astronomy, University of Maryland, College Park, MD 20742, USA
                                                          <sup>21</sup> Joint Space-Science Institute, University of Maryland, College Park, MD 20742, USA
                               <sup>22</sup> Astrophysics Science Division, NASA Goddard Space Flight Center, 8800 Greenbelt Rd., Greenbelt, MD 20771, USA
                                                Received 2025 February 11; revised 2025 May 28; accepted 2025 May 29; published 2025 August 5
```

Abstract

We present the optical discovery and multiwavelength follow-up observations of AT 2024kmq, a likely tidal disruption event (TDE) associated with a supermassive ($M_{\rm BH} \sim 10^8 \, M_{\odot}$) black hole in a massive galaxy at z=0.192. The optical light curve of AT 2024kmq exhibits two distinct peaks: an early fast (timescale 1 day) and luminous ($M\approx -20$ mag) red peak, then a slower (timescale 1 month) blue peak with a higher optical luminosity ($M\approx -22$ mag) and featureless optical spectra. The second component is similar to the spectroscopic class of "featureless TDEs" in the literature, and during this second component we detect highly variable, luminous ($L_{\rm X}\approx 10^{44}\,{\rm erg\,s^{-1}}$), and hard ($f_{\nu}\propto \nu^{-1.5}$) X-ray emission. Luminous ($10^{29}\,{\rm erg\,s^{-1}\,Hz^{-1}}$ at 10 GHz) but unchanging radio emission likely arises from an underlying active galactic nucleus. The luminosity, timescale, and color of the early red optical peak can be explained by synchrotron emission, or alternatively by thermal emission from material at a large radius ($R\approx a$ few \times $10^{15}\,{\rm cm}$). Possible physical origins for this early red component include an off-axis relativistic jet, and shocks from self-intersecting debris leading to the formation of the accretion disk. Late-time radio observations will help distinguish between the two possibilities.

Unified Astronomy Thesaurus concepts: Time domain astronomy (2109); Transient sources (1851); Surveys (1671)

Materials only available in the online version of record: machine-readable table

1. Introduction

The tidal disruption and accretion of a star by a black hole can produce a luminous electromagnetic transient (J. G. Hills 1975; M. J. Rees 1988; see S. Komossa 2015 and S. Gezari 2021 for recent reviews). Wide-field time-domain surveys such as the Zwicky Transient Facility (ZTF;

Original content from this work may be used under the terms of the Creative Commons Attribution 4.0 licence. Any further distribution of this work must maintain attribution to the author(s) and the title of the work, journal citation and DOI.

E. C. Bellm et al. 2019b; M. J. Graham et al. 2019) in the optical band have enabled large-scale systematic studies of tidal disruption events (TDEs), with over 100 discovered to date, and the delineation of several spectroscopic classes (S. Gezari 2021; S. van Velzen et al. 2021; E. Hammerstein et al. 2023; Y. Yao et al. 2023). Major open questions in the TDE field include how the accretion disk forms following the disrupted star's return to pericenter (G. Lodato et al. 2015; C. Bonnerot & N. C. Stone 2021), and under what circumstances the accretion process leads to the launch of a relativistic jet (F. De Colle & W. Lu 2020).

Typically, the optical emission observed in TDEs is blue (thermal with $T_{\rm BB} \sim 10^4\,\rm K$) and evolves on a timescale of weeks to months (S. Gezari 2021). The powering mechanism for the optical emission is uncertain: possibilities include accretion onto the black hole (e.g., L. E. Strubbe & E. Quataert 2009), shocks from self-intersecting debris streams (e.g., T. Piran et al. 2015), and reprocessing of soft X-rays (e.g., N. Roth et al. 2016). However, one TDE was recently discovered via rapidly fading, red, nonthermal optical emission (AT 2022cmc; I. Andreoni et al. 2022). The optical emission—alongside luminous X-ray and radio emission—has been interpreted as synchrotron radiation from the afterglow of an on-axis jet (I. Andreoni et al. 2022; D. R. Pasham et al. 2023).

AT 2022cmc is one of only four on-axis jetted TDEs discovered to date (see F. De Colle & W. Lu 2020 for a review); the other three (J. S. Bloom et al. 2011; D. N. Burrows et al. 2011; A. J. Levan et al. 2011; B. A. Zauderer et al. 2011; S. B. Cenko et al. 2012; G. C. Brown et al. 2015) were identified as high-energy transients by the Burst Alert Telescope (S. D. Barthelmy et al. 2005) on the Neil Gehrels Swift Observatory (Swift; N. Gehrels et al. 2004). Two of the on-axis jetted TDEs, including AT 2022cmc, had optical properties closely resembling those of the rare class of "featureless TDEs," which are characterized by high optical luminosities ($-23 \lesssim M_{\rm peak} \lesssim -21$ mag) and featureless optical spectra (E. Hammerstein et al. 2023). The observed association led I. Andreoni et al. (2022) to suggest a link between featureless TDEs and the presence of a relativistic jet.

In addition, several TDEs in the literature have exhibited double-peaked optical light curves (T. W. S. Holoien et al. 2019; S. Faris et al. 2024; S. Huang et al. 2024; Y. Wang et al. 2024). For example, AT 2023lli had a monthlong "bump" 2 months prior to the peak of the optical light curve (S. Huang et al. 2024). ASASSN-19bt exhibited a short (dayslong to weekslong) luminosity spike, identified by fitting the spectral energy distribution (SED) of the ultraviolet (UV) and optical data (T. W. S. Holoien et al. 2019). The early bumps have typically been blue in color. Their origin is uncertain, but one possibility is that they arise from the self-intersection of the stream debris (S. Huang et al. 2024).

In this paper we present AT 2024kmq, a second TDE identified on the basis of early fast red optical emission that also had the longer-lasting thermal component characteristic of featureless TDEs. The X-ray luminosity of AT 2024kmq is intermediate between "ordinary" optical TDEs and on-axis jetted TDEs, and there is no clear radio emission from the transient itself, although deep constraints are difficult owing to luminous radio emission that is likely from the active galactic nucleus (AGN) of the host galaxy. We present the discovery and observations in Section 2, basic inferences and comparisons to known TDEs in Section 3, the modeling of the first optical peak in Section 4, and a summary in Section 5. This paper focuses on data obtained of this transient prior to 2024 October, when observations became limited by a Sun constraint. A subsequent paper (Y. Yao et al. 2025, in preparation) will focus on our late-time observations.

We adopt a standard Λ CDM cosmology with matter density $\Omega_M = 0.31$ and the Hubble constant $H_0 = 67.7 \, \mathrm{km \, s^{-1} \, Mpc^{-1}}$ (Planck Collaboration et al. 2020). Unless otherwise noted, uncertainties are reported using 68% confidence intervals and upper limits are reported at 3σ .

2. Observations and Analysis

2.1. Transient Identification and TDE Classification

AT 2024kmq was detected as ZTF 24aapvieu on 23 2024 June 1 05:21:18 at $g=19.93\pm0.08$ mag 24 at $\alpha=12^{\rm h}02^{\rm m}37\26 , $\delta=+35^{\circ}23'35.''5$ (J2000) as part of the ZTF high-cadence partnership survey (E. C. Bellm et al. 2019a) with the 48 inch Samuel Oschin Schmidt telescope at Palomar Observatory (P48). The ZTF observing system is described in R. Dekany et al. (2020) and the data processing pipeline is described in F. J. Masci et al. (2019). The identification of AT 2024kmq made use of machine learning based real–bogus classifiers (D. A. Duev et al. 2019; A. Mahabal et al. 2019) and a star–galaxy separator (Y. Tachibana & A. A. Miller 2018). AT 2024kmq was also detected by the Gravitational-wave Optical Transient Observer (GOTO; M. J. Dyer et al. 2024) \sim 1 day prior to the first ZTF detection, on 2024 May 30 21:16:09.

Upon the first ZTF detection on 2024 June 1, AT 2024kmq passed a filter designed to identify rapidly brightening luminous transients (e.g., A. Y. Q. Ho et al. 2020). The rise rate was 0.5 mag day in the g band from a nondetection two nights prior. The ZTF transient position was a 0.5 offset from the nucleus of the cataloged galaxy SDSS J120237.22 +352335.3. From the Sloan Digital Sky Survey (SDSS) photometric redshift of $z_{\rm ph}=0.231\pm0.014$ (R. Beck et al. 2016), the implied peak luminosity of the transient was \approx -20.4 mag. Over the next two nights, daily ZTF data showed fading of almost 1 mag in the g band, implying that this was a short-duration transient. The optical light curve is shown in Figure 1.

To confirm the rapid decline, we triggered imaging observations (described in more detail in Section 2.2) using the Spectral Energy Distribution Machine (SEDM; N. Blagorodnova et al. 2018; M. Rigault et al. 2019; Y. L. Kim et al. 2022) on the automated 60 inch telescope at Palomar Observatory (P60; S. B. Cenko et al. 2006), and the Large Monolithic Imager (LMI) on the Lowell Discovery Telescope (LDT). Imaging obtained on 2024 June 6 showed fast fading from the ZTF detections. In addition, the LDT imaging revealed red colors (g - r = 0.6 mag, corrected for an $A_V = 0.054$ Milky Way extinction²⁶; E. F. Schlafly & D. P. Finkbeiner 2011), distinguishing AT 2024kmq from the typically blue colors of extragalactic day-timescale transients (M. R. Drout et al. 2014; M. Pursiainen et al. 2018; A. Y. Q. Ho et al. 2023).

To measure the transient redshift, on 2024 June 7 we triggered a Target of Opportunity (ToO) program²⁷ using the Gemini Multi-object Spectrograph (GMOS; I. M. Hook et al. 2004) on Gemini North (more details in Section 2.3). We also reported the event to the Transient Name Server (J. Vail et al. 2024). As discussed in J. Sevilla et al. (2024), the GMOS spectrum was dominated by the host galaxy. Detections of Na I, Mg I, H α , and H β absorption lines yielded a

²³ All times given in UTC.

²⁴ All magnitudes given in AB.

²⁵ Subsequent deeper optical imaging suggests that the transient is in fact nuclear; see Section 2.2.

²⁶ The UV and optical SED of the second component in the optical light curve is typical of TDEs, suggesting minimal host-galaxy extinction; see Section 3.4 for more details.

²⁷ Program ID GN-2024A-Q-127, PI: Ho.

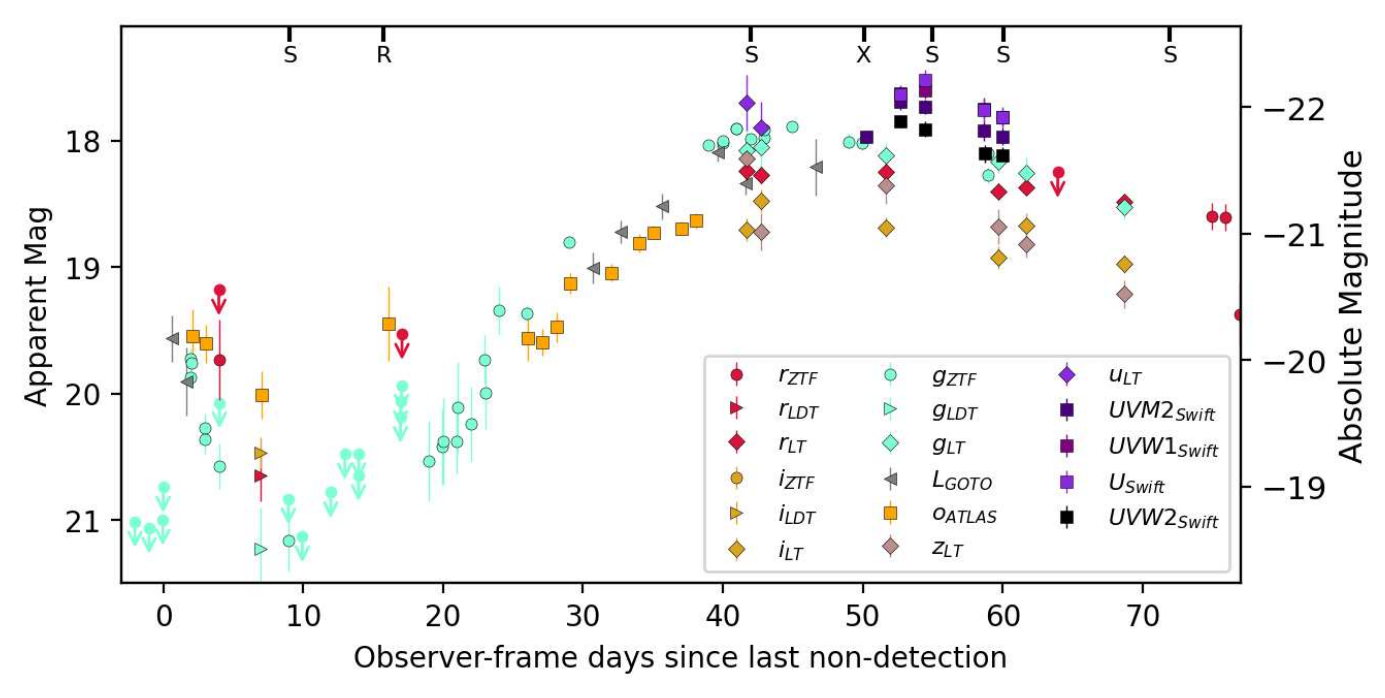


Figure 1. Select optical and UV photometry of AT 2024kmq (corrected for Milky Way extinction) with epochs of key follow-up observations marked: S for spectroscopy, R for the first radio observation, and X for the first X-ray observation. The absolute magnitude has a cosmological correction of $2.5 \log_{10}(1+z)$ applied. Upper limits (5σ) are marked with downward-facing arrows.

spectroscopic redshift of z = 0.192 and an implied absolute peak magnitude (with a cosmological correction; $M = m_{\rm obs} - 5\log_{10}(D_L/10~{\rm pc}) + 2.5\log_{10}(1+z)$) of $M_g = -19.97 \pm 0.08$ mag. The lack of any emission lines in the host galaxy was unusual for a fast extragalactic transient (P. Wiseman et al. 2020) but not unprecedented (M. Nicholl et al. 2023). Due to the confirmed high optical luminosity, we triggered a radio ToO program using the Karl G. Jansky Very Large Array (VLA); the radio observations are described in more detail in Section 2.6.

Starting on 2024 June 18, the ZTF *g*-band light curve showed significant rebrightening over a timescale of weeks, motivating us to pursue a multiwavelength observing campaign. We classify AT 2024kmq as a TDE based on the persistent blue color and hot photospheric temperature of the second (primary) peak, the featureless optical spectra, and the mass and color of its host galaxy (Section 2.4.1), which are all reminiscent of the TDE-featureless spectral subtype (E. Hammerstein et al. 2023).

Throughout the paper we use the time of the last ZTF nondetection ($t_0 = 60460.24495$ MJD) as our reference epoch, which is 0.64 days prior to the first GOTO detection. Follow-up observations were coordinated using the SkyPortal (S. van der Walt et al. 2019; M. W. Coughlin et al. 2023) platform.

2.2. Ground-based Optical Photometry

Our optical photometry of AT 2024kmq is summarized in Table 5 in Appendix A. We obtained six epochs of multiband Liverpool Telescope (LT; I. A. Steele et al. 2004) IO:O photometry of AT 2024kmq. We performed astrometric alignment on images that had been reduced using the standard LT pipeline. Image subtraction was conducted using the Pan-STARRS1 Surveys (PS1; K. C. Chambers et al. 2016) imaging catalog as a reference and a custom IDL routine (the PS1 image was convolved to match the point-spread function (PSF)

of the LT image, then subtracted). Transient photometry was performed using seeing-matched aperture photometry fixed at the transient location and calibrated relative to a set of SDSS secondary standard stars in the field (as measured from the unsubtracted images). We performed photometry in the same way for the single epoch of LDT/LMI imaging and the four epochs of P60/SEDM imaging. We added (0.3, 0.2, 0.1 mag) of systematic uncertainty in quadrature to the (g, r, i)-band LDT/LMI data. PSF-fit forced photometry was performed on archived difference images from the ZTF survey using the ZTF forced-photometry service (F. J. Masci et al. 2023). We also obtained forced photometry from the Asteroid Terrestrial-impact Last Alert System (ATLAS) forced-photometry service (J. L. Tonry et al. 2018b; K. W. Smith et al. 2020), which we binned in timescales of 1 day.

The GOTO (M. J. Dyer et al. 2024) data were observed as part of routine sky-survey operations in the GOTO L band (\sim 400–700 nm) and reduced in real time via an internal pipeline (J. Lyman et al. 2025, in preparation). Forced photometry was performed in small apertures on difference images at the location of AT 2024kmq via the GOTO light-curve service (D. Jarvis et al. 2025, in preparation). These small-aperture measurements were corrected for missing flux using a local measurement of the aperture correction from nearby bright stars. Image-level zero-points were calculated using ATLAS-REFCAT2 (J. L. Tonry et al. 2018a), with a position-dependent correction to the image-level value applied, again using bright stars in the field.

The position of the optical transient as measured by LDT is consistent with the host-galaxy nucleus. More specifically, in the r band, which has the cleanest subtraction, the offset of the transient from the host-galaxy nucleus is $[0\%045, 0\%137] \pm [0\%114, 0\%132]$ in the [E, N] direction. The uncertainty in the position is the rms astrometric scatter in the offsets of the other

 Table 1

 Spectroscopic Observations of AT 2024kmq

Start Date (MJD)	Δt (days)	Telescope+Instrument	Exposure Time (seconds)
60469.3026	9	Gemini+GMOS	450
60502.2383	42	P200+DBSP	900
60515.1906	55	P200+DBSP	600
60520.2666	60	Keck1+LRIS	605
60532.1814	72	Shane+KAST	720

Note. Observer-frame epochs given since t_0 as defined in Section 2.1.

objects in the image. We note that at the redshift of AT 2024kmq, 0".1 corresponds to 0.3 kpc.

Finally, we searched for historical flaring at the transient position. Forced photometry on ZTF images²⁸ (F. J. Masci et al. 2023) extending back to the start of the survey did not show any clear transient event. In the AllWISE catalog, the source is categorized as likely nonvariable in the W1 and W2 filters (R. M. Cutri et al. 2021).

2.3. Optical Spectroscopy

We obtained five optical spectra of AT 2024kmq. The epochs of spectroscopic observations are marked with "S" in Figure 1, and observation details are provided in Table 1. The spectral sequence is shown in Figure 2.

The first spectrum was obtained using GMOS with the R400 grating and a 1" wide slit, which gives a resolution of 959 at the blaze wavelength of 764 nm. We reduced the GMOS spectrum using the PypeIt package (J. X. Prochaska et al. 2020). We obtained two spectra using the Double Beam Spectrograph (DBSP; J. B. Oke & J. E. Gunn 1982) on the 200 inch Hale telescope at Palomar Observatory. We used the 600/ 4000 grating for the blue arm and the 316/7500 grating for the red arm, covering 3200-10000 Å at an average resolution of \sim 1000. The slit was oriented along the parallactic angle. We reduced the data using the P200/DBSP pipeline described in M. Roberson et al. (2022). We obtained one spectrum using the Low Resolution Imaging Spectrometer (LRIS; J. B. Oke et al. 1995) on the Keck I 10 m telescope and a final spectrum using the Kast spectrograph on the Shane 3 m telescope at Lick Observatory. For the LRIS observation we used a 1" wide slit, a 400/8500 grating (red-side CCD), and a 400/3400 grism (blue-side CCD). For the Kast observation we used the 300/ 7500 grating (red-side CCD, 2.55 Å pixel⁻¹ dispersion) and 600/4310 grism (blue-side CCD, 1.02 Å pixel⁻¹ dispersion), with a slit width of 1.5. The Keck/LRIS pipeline Lpipe is described in D. A. Perley (2019), and the KAST spectrum was reduced using the UCSC Spectral Pipeline (M. R. Siebert et al. 2019).

The first spectrum was obtained at the end of the early red peak (see Figure 1), and is dominated by the host galaxy. The remaining spectra were obtained during the second peak, when the transient had rebrightened, and are dominated by a featureless blue continuum. It is on the basis of these later spectra that we classify AT 2024kmq as a featureless TDE (E. Hammerstein et al. 2023). To search for broad lines from the transient, we scaled and subtracted a model spectrum of the

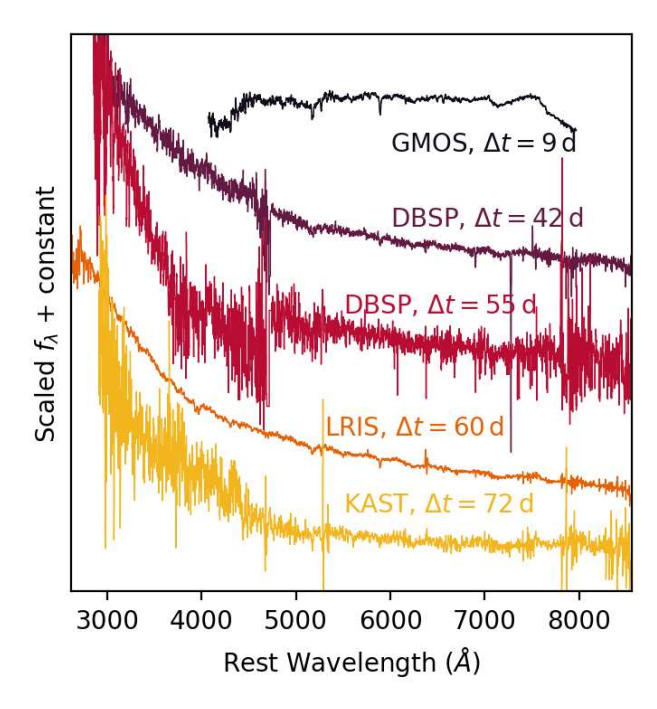


Figure 2. The optical spectra of AT 2024kmq, binned using 3–6 Å bins. The observer-frame epoch is given with respect to t_0 as defined in Section 2.1. No host-galaxy subtraction has been performed, so the first spectrum is dominated by features from the host galaxy.

host galaxy (Section 3.1) from the first spectrum at $\Delta t = 9$ days (Figure 3, top panel). In addition, we fit the flux-calibrated LRIS spectrum at $\Delta t = 60$ days to a model that includes both a blackbody and the host galaxy (Figure 3, bottom panel). We did not identify any clear broad lines from the transient itself.

2.4. Swift

AT 2024kmq was observed by the Ultraviolet/Optical Telescope (UVOT; P. W. A. Roming et al. 2005) and the X-Ray Telescope (XRT; D. N. Burrows et al. 2005) on board Swift for five epochs (total exposure time: 7.4 ks) from 2024 July 19 to 2024 July 29.

2.4.1. UVOT

The UVOT flux of AT 2024kmq was measured with uvotsource, using a circular source region with $r_{\rm src}=5''$. The background flux was measured using four nearby circular source-free regions with $r_{\rm bkg}=6''$. We estimated the hostgalaxy flux by fitting a host-galaxy synthesis model on archival photometry from the Galaxy Evolution Explorer (GALEX), SDSS, and the Wide-field Infrared Survey Explorer (WISE) (more details in Section 3.1). The best-fit model gives observed host-galaxy magnitudes of $uvw2=25.43\,{\rm mag},$ $uvm2=26.02\,{\rm mag},$ $uvw1=23.75\,{\rm mag},$ $uvw2=25.43\,{\rm mag},$ uv

The data is available at IPAC (IRSA 2022).

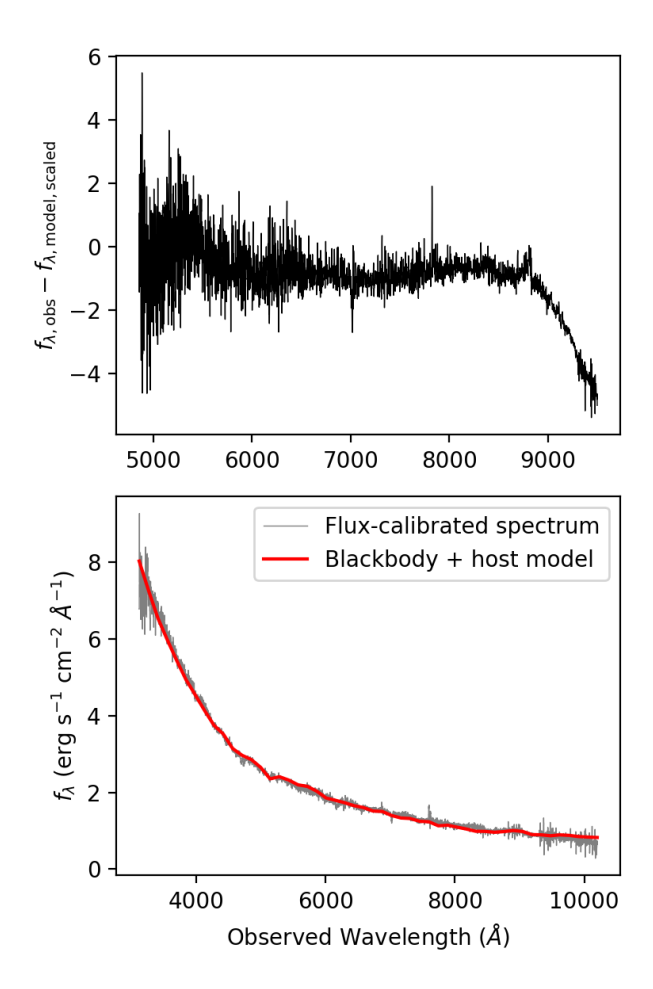


Figure 3. Top: the observed GMOS spectrum (at $\Delta t = 9$ days) with the host-galaxy model spectrum subtracted. There are no clear broad features from the transient. Bottom: the flux-calibrated LRIS spectrum (at $\Delta t = 60$ days, gray) with a best-fit blackbody model summed together with the host-galaxy model (red). The parameters of the blackbody model are $R = 2.6 \times 10^{15}$ cm and T = 18,000 K, very similar to the parameters inferred from the photometry.

2.4.2. XRT

We processed the XRT data using HEASoft version 6-33.2. The source was detected in all five obsIDs. We identified no significant hardness evolution across the obsIDs. We created an X-ray light curve per good time interval (GTI), then grouped adjacent GTIs within a single obsID together if the change in count rate was less than 1σ , resulting in six time bins.

To generate the time-averaged source and background XRT spectra, we stacked the cleaned event files with xselect, and filtered them using a source region with $r_{\rm src}=40''$, and eight background regions with $r_{\rm bkg}=45''$ evenly spaced at 100'' from AT 2024kmq. The source spectrum was grouped with ftgrouppha using the optimal binning scheme developed by J. S. Kaastra & J. A. M. Bleeker (2016), requiring at least one count per bin.

Using *C*-statistics (W. Cash 1979), we modeled the spectrum with an absorbed power law (tbabs*zashift*-powerlaw in xspec). The redshift was fixed at z=0.192 and the hydrogen-equivalent column density $N_{\rm H}$ was fixed at the Galactic value of $1.77 \times 10^{20} \, {\rm cm}^{-2}$ (R. Willingale et al. 2013). The best-fit model (see Figure 4) yielded a power-law photon index of $\Gamma=2.45\pm0.20$, cstat/degrees of

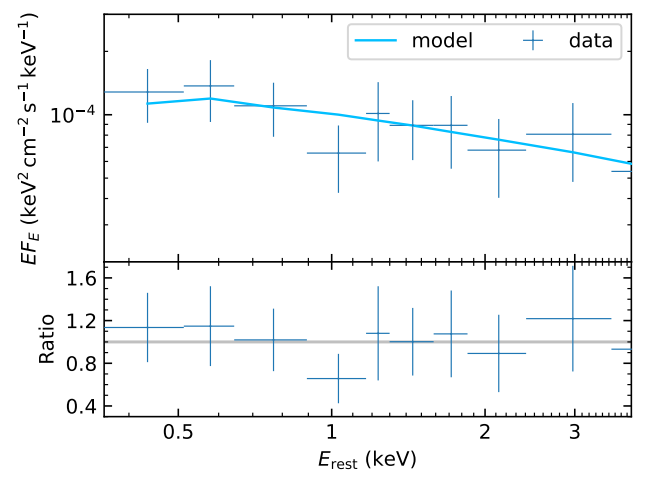


Figure 4. Top: XRT stacked spectrum of AT 2024kmq, overplotted with the best-fit absorbed power-law model. Bottom: the ratio of data to the best-fit model. The data have been rebinned for visual clarity.

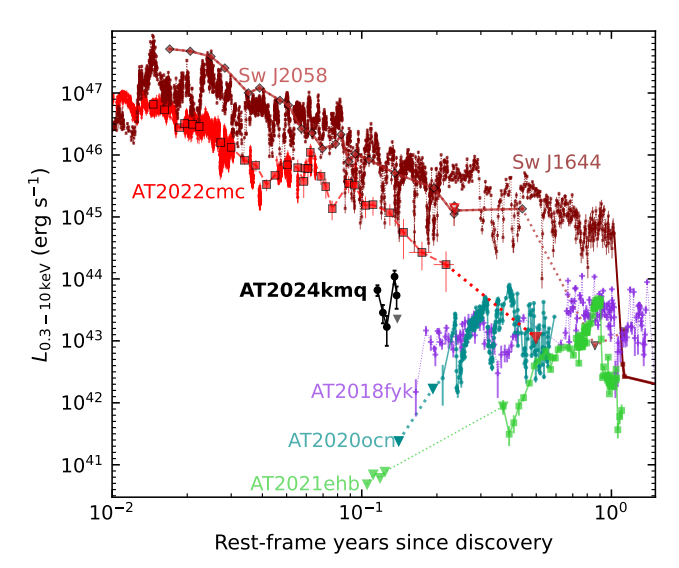


Figure 5. The X-ray light curve of AT 2024kmq compared with the X-ray light curves of TDEs that exhibit significant hard X-ray emission (D. R. Pasham et al. 2015, 2024; V. Mangano et al. 2016; T. Eftekhari et al. 2018, 2024; T. Wevers et al. 2021; Y. Yao et al. 2022, 2024).

Table 2Swift/XRT Observations of AT 2024kmq

MJD	Δt (days)	Exp. (s)	$f_{\rm X}$ (10 ⁻¹³ erg s ⁻¹ cm ⁻²)	$L_{\rm X}$ (10 ⁴³ erg s ⁻¹)
60510.3208	49	1988	6.28 ± 1.23	6.59 ± 1.29
60512.9092	52	1903	2.72 ± 0.89	2.86 ± 0.94
60514.8491	54	1608	1.60 ± 0.81	1.68 ± 0.85
60518.9262	58	759	10.36 ± 2.60	10.87 ± 2.72
60520.0460	59	705	5.16 ± 2.02	5.41 ± 2.12
60520.4383	60	463	< 2.18	< 2.29

Note. f_X and L_X are given in the 0.3–10 keV energy range.

freedom = 11.51/21, and an observed 0.3–10 keV flux of $4.37^{+0.58}_{-0.51} \times 10^{-13}\,\mathrm{erg}\,\mathrm{s}^{-1}\,\mathrm{cm}^{-2}$. The 0.3–10 keV net count rate to flux conversion factor was found to be $3.86\times 10^{-11}\,\mathrm{erg}\,\mathrm{count}^{-1}\,\mathrm{cm}^{-2}$. The list of XRT observations is given in Table 2 and the X-ray light curve is shown in Figure 5.

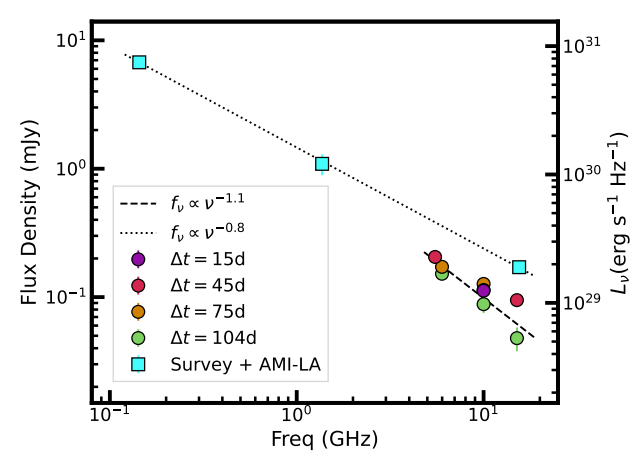


Figure 6. The SED of a radio source consistent with the nucleus of the AT 2024kmq host galaxy. Circles mark VLA data presented in this paper. Squares mark survey data (LOFAR and ASKAP) from prior to the optical transient, as well as AMI-LA data from $\Delta t = 55$ days.

2.5. eROSITA

The position of AT 2024kmq was observed by the eROSITA telescope (P. Predehl et al. 2021) on board the Spektr-RG (SRG) satellite (R. Sunyaev et al. 2021). The position was observed in four epochs from 2020 to 2022, each separated by 6 months, with the first observation held on 2020 May 27 (MJD 58996.43). The 0.2–2.3 keV upper limit is $\sim\!\!4\times10^{-14}\,\mathrm{erg\,s^{-1}\,cm^{-2}}$ in individual scans, and $\sim\!\!1.5\times10^{-14}\,\mathrm{erg\,s^{-1}\,cm^{-2}}$ in the combined data of all four observations. The latter upper limit corresponds to $L_{\rm X}<1.6\times10^{42}\,\mathrm{erg\,s^{-1}}$. Therefore, the X-ray emission observed by XRT is clearly dominated by the transient.

2.6. Radio

2.6.1. VLA

We obtained four epochs of observations of AT 2024kmq²⁹ from MJD 60475.98 to 60565.03 (15.09–140.14 days post discovery) with the VLA (R. A. Perley et al. 2011), at mean frequencies of 6, 10, and 15 GHz. The quasar 3C 286 was used as the flux density and bandpass calibrator and J1215+3448 as the complex gain calibrator and all observations were taken in B configuration. The data were calibrated and imaged under the Science Ready Data Products (SRDP) initiative,³⁰ which uses the Common Astronomy Software Applications (CASA; J. P. McMullin et al. 2007) VLA Calibration Pipeline³¹ and VLA Imaging Pipeline.³² We downloaded the regularly calibrated continuum images for each epoch and mean frequency.

There is a clear radio source detected at the position of the host-galaxy nucleus. To determine the flux density and shape of the source, we used the pwkit/imtool program (P. K. G. Williams et al. 2017). We did not find a significant difference in the inferred flux density when modeling the source as pointlike or extended, so for consistency we

measured the flux density for all epochs assuming a pointlike source. The results of this analysis are presented in Table 6 in Appendix A and in Figure 6. Due to the limited variability and the archival detection of extended radio emission (Section 2.6.2), we conclude that the radio emission likely arises from an AGN in the host galaxy, and is unassociated with the transient (more details in Section 3.1).

We note that a radio source at the position of AT 2024kmq was detected by the Arcminute Microkelvin Imager Large Array (AMI-LA) on 2024 July 25 (55 days post detection) at a mean frequency of 15.5 GHz and a flux density of $f_{\nu}=0.171\pm0.020$ mJy (A. Lang et al. 2024). This is \sim 2 times brighter than the VLA observations encompassing the AMI-LA observations at 45 and 75 days. The discrepancy could potentially be due to the source being extended (Section 3.5).

For the remainder of the paper we adopt the measured point-source brightness of the AGN (\approx 0.1 mJy at 10 GHz) as the upper limit on the brightness of the AT 2024kmq transient emission.

2.6.2. Archival Radio Imaging

We utilized the Low-frequency Array (LOFAR) Twometer Sky Survey (LoTSS) Data Release 2 cutout API to generate a cutout³³ at the position of AT 2024kmq (T. W. Shimwell et al. 2022). There is a clearly detected and extended source at the position of AT 2024kmq, coincident with the VLA radio source; imtool prefers an extended profile (approximate size of $14.1^{''} \times 8.6$, compared to a beam size of $6'' \times 6''$) for this source, and we measured a flux density of $f_{\nu} = 6.74 \pm 0.22$ mJy (compared to only $f_{\nu} = 2.34 \pm 0.62$ mJy when the shape is forced to be pointlike) at a mean frequency of 150 MHz. Similarly, we utilized the CSIRO Australian Square Kilometre Array Pathfinder (ASKAP) Science Data Archive (CASDA) Cutout Service to generate a Rapid ASKAP Continuum Survey-Mid (RACS-Mid) cutout from an observation taken on 2020 December 24 (S. W. Duchesne et al. 2023). At the position of AT 2024kmq we measured a flux density of $f_{\nu} = 1.09 \pm 0.20$ mJy at a mean frequency of 1.4 GHz. The extended size inferred from the LoTSS imaging corresponds to \approx 50 kpc at the distance of AT 2024kmq, which is typical for radio-loud AGN (M. J. Hardcastle et al. 2019).

3. Basic Properties and Inferences

3.1. Host Galaxy

As mentioned in Section 2.4.1, we fit a host-galaxy model to the GALEX, SDSS, and WISE photometry following the same procedures adopted by S. van Velzen et al. (2021) and E. Hammerstein et al. (2023). Specifically, we used Prospector (B. D. Johnson et al. 2021), the Markov Chain Monte Carlo sampler emcee (D. Foreman-Mackey et al. 2013), and the Flexible Stellar Population Synthesis (FSPS) models (C. Conroy et al. 2009). The best-fit host-galaxy properties are given in Table 3.

In Figure 7, we compare the stellar mass and the Galactic extinction–corrected, synthetic rest-frame u-r color of the host galaxy of AT 2024kmq to those of known ZTF TDEs. The

²⁹ Programs 23B-138 (PI: A. Ho) and 24A-494 (PI: Y. Yao).

³⁰ https://science.nrao.edu/srdp

³¹ https://science.nrao.edu/facilities/vla/data-processing/pipeline

³² https://science.nrao.edu/facilities/vla/data-processing/pipeline/vipl_ 661_v2

³³ The cutout header does not have an observation date, but all of the observations for LoTSS DR2 were taken before the first optical detection of AT 2024kmq.

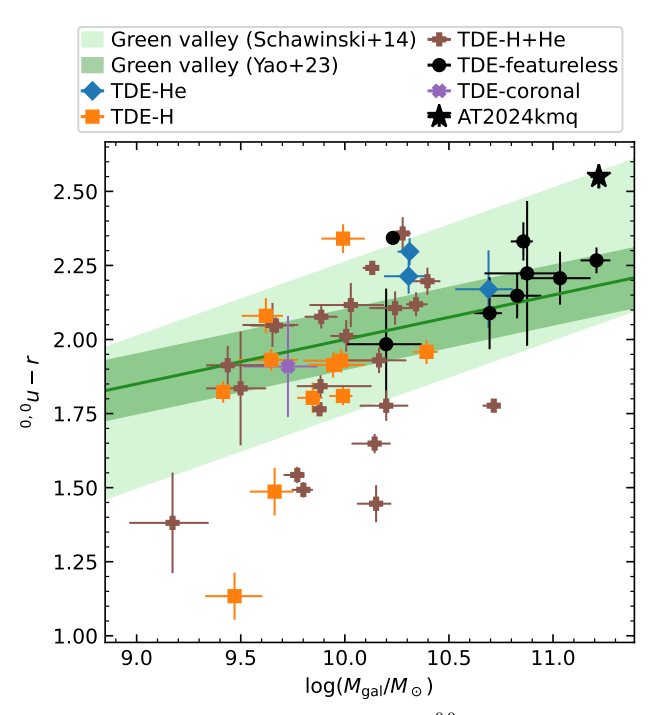


Figure 7. The host galaxy of AT 2024kmq on the $^{0.0}u-r$ vs. $M_{\rm gal}$ diagram, compared with published ZTF TDE samples color-coded by the optical spectral subtype (S. van Velzen et al. 2021; E. Hammerstein et al. 2023; Y. Yao et al. 2023). Green bands mark the green valley defined by K. Schawinski et al. (2014) and Y. Yao et al. (2023).

comparison sample of 45 TDEs was constructed by combining all events presented by S. van Velzen et al. (2021), E. Hammerstein et al. (2023), and Y. Yao et al. (2023) that have a known optical spectral subtype. The host-galaxy properties were measured in the same fashion (Prospector and FSPS). As can be seen, the host galaxy of AT 2024kmq is most similar to previously known featureless TDEs, which are found to be preferentially hosted by high-mass galaxies. We note that the 95% confidence upper limit on the host-galaxy mass of AT 2022cmc is $\log(M/M_{\odot}) < 11.2$ (I. Andreoni et al. 2022).

The $M_{\rm gal}$ – $M_{\rm BH}$ scaling relation presented in J. E. Greene et al. (2020), which was derived using all galaxies with dynamical measurements and upper limits on $M_{\rm BH}$, implies a black hole mass for AT 2024kmq of $\log(M_{\rm BH}/M_{\odot})=8.63\pm0.83$. The $M_{\rm gal}$ – $M_{\rm BH}$ scaling relation derived in Y. Yao et al. (2023) using 19 TDE hosts with velocity dispersion measurements implies a black hole mass of $\log(M_{\rm BH}/M_{\odot})=8.54\pm0.37$.

Using the GMOS spectrum (Section 2.3), we measured the stellar velocity dispersion (σ_*) of the host galaxy using pPXF (M. Cappellari & E. Emsellem 2004; M. Cappellari 2017). Following the procedures adopted by Y. Yao et al. (2023), we obtained $\sigma_* = 175.4^{+27.0}_{-26.9}$ km s⁻¹. Using the J. Kormendy & L. C. Ho (2013) $M_{\rm BH}$ – σ_* scaling relation, this implies a black hole mass of $\log(M_{\rm BH}/M_\odot) = 8.24 \pm 0.30 ({\rm stat}) \pm 0.29 ({\rm sys})$.

If the disrupted star is a Sun-like star, the Hills mass³⁴ is only above $4 \times 10^8 M_{\odot}$ for a highly spinning black hole with spin parameter $a_{\rm BH} \gtrsim 0.95$ (see, e.g., Figure 4 of G. Leloudas et al. 2016). If the disrupted star is a higher-mass main-

 Table 3

 Best-fit Host-galaxy Properties of AT 2024kmq

Parameter	Value
$\log(M_{ m gal}/M_{\odot})$	$11.22^{+0.03}_{-0.04}$
$^{0,0}u-r$ (mag)	2.55 ± 0.04
$E_{B-V,\mathrm{host}}$ (mag)	$0.06^{+0.08}_{-0.04}$
t_{age} (Gyr)	$11.21^{+0.97}_{-1.52}$
$\tau_{\rm sfh}$ (Gyr)	$0.30_{-0.16}^{+0.37}$
$\log(Z/Z_{\odot})$	$-0.10^{+0.08}_{-0.10}$

sequence or evolved star, smaller values of $a_{\rm BH}$ are allowed. We note that $M_{\rm gal}$ – $M_{\rm BH}$ relations do have significant scatter: early-type galaxies in J. E. Greene et al. (2020) with $M_{\rm gal} \sim 10^{11}\,M_{\odot}$ have black hole masses down to $10^7\,M_{\odot}$. So, we cannot rule out the possibility that the black hole mass in AT 2024kmq is closer to $10^7\,M_{\odot}$. However, it is likely that most featureless TDEs have black holes of $M_{\rm BH} \approx 10^8\,M_{\odot}$.

This point could be clarified by saying that the AGN emission is relatively weak in the preflare optical spectrum, then followed by a discussion on the effect of mid-infrared (MIR) emission.

The luminous and relatively unvarying radio emission (Section 2.6) suggests that the host galaxy of AT 2024kmq harbors an AGN, which we discuss in further detail in Section 3.5. The AGN is likely to contribute only at MIR and longer wavelengths, as the AGN emission is weak in the preflare optical spectrum. These wavelengths are typically not very sensitive to the mass of the galaxy, as they trace reprocessed emission via dust. To confirm that the AGN contribution does not affect the mass of the galaxy inferred from our SED fitting, we also performed the SED fit excluding the WISE photometry.

3.2. Origin of Early-time Hard X-Ray Emission

In general, although a significant fraction (at least 40%) of optically selected TDEs eventually exhibit $>10^{42}\,\mathrm{erg\,s^{-1}}$ X-ray emission, luminous ($10^{44}\,\mathrm{erg\,s^{-1}}$) X-ray emission at the time of the optical peak is rare (e.g., M. Guolo et al. 2024). While most TDEs exhibit thermal soft X-ray emission originating from the inner accretion disk, dominant nonthermal hard X-rays (Γ < 3) have so far only been observed in two small groups of TDEs (see Figure 5): those with on-axis jets and those with a late-time soft-to-hard spectral transition at a few $\times 10^2$ days after the optical peak. The former group features prompt, very luminous ($\sim 10^{47} \, \mathrm{erg \, s^{-1}}$) hard X-ray emission powered by internal energy dissipation within an onaxis jet (D. N. Burrows et al. 2011; Y. Yao et al. 2024). The latter group includes AT 2018fyk (T. Wevers et al. 2021), AT 2021ehb (Y. Yao et al. 2022), and AT 2020ocn (D. R. Pasham et al. 2024). Their X-rays are attributed to corona emission and their spectral hardening has been explained by the gradual formation of a magnetically dominated corona above the newly formed accretion disk, where inverse Compton scattering of thermal seed photons in the corona produces the power-law X-ray spectra.

The X-ray properties of AT 2024kmq are different from the properties of the above two groups. It developed hard X-rays at an early phase, no later than the primary optical peak, but at a luminosity that is much fainter than that of on-axis jetted TDEs. We consider two possibilities for the origin of its hard

³⁴ The Hills mass is defined as the maximum black hole mass for an observable TDE where the tidal radius is outside of the event horizon radius (J. G. Hills 1975).

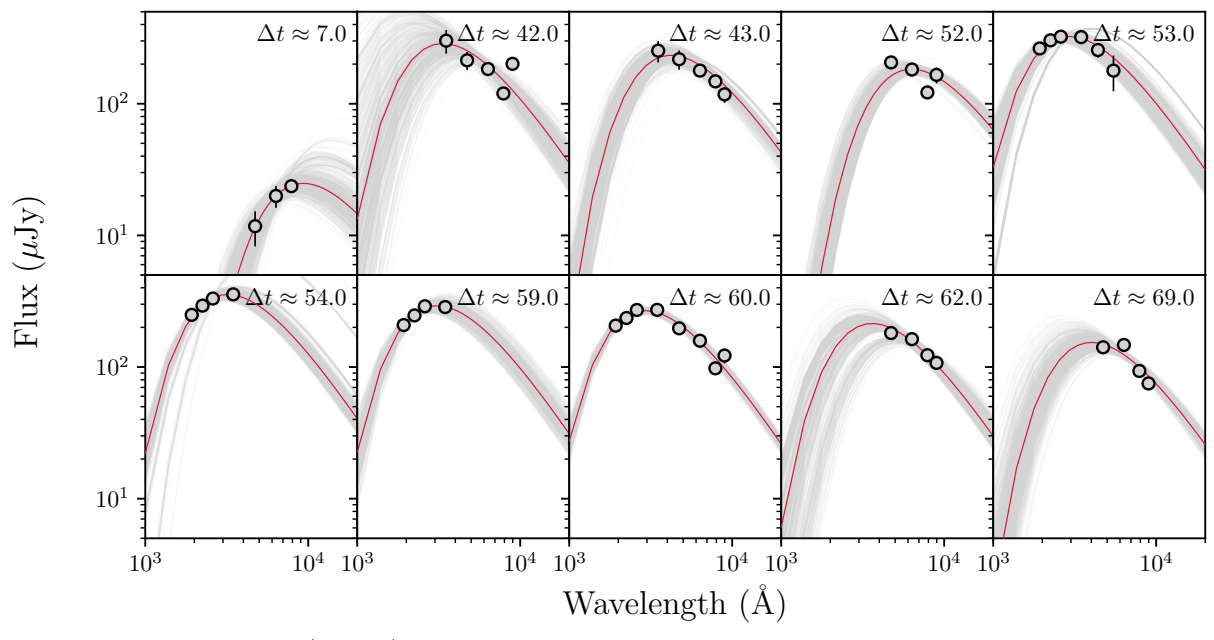


Figure 8. Blackbody fits to the LDT, LT, and/or Swift/UVOT SEDs of AT 2024kmq. Epochs are given in days from the last optical nondetection. The gray lines show each of the 600 fits, and the red line shows the median value. LT observations at $\Delta t = 41$ days and $\Delta t = 51$ days were hampered by bad seeing.

X-rays: a jet viewed off-axis (Section 4.1), and the inner accretion disk (Section 4.2) provided that Comptonization is efficient.³⁵

3.3. Search for Early Luminous Red Components in TDE Light Curves

As discussed in Section 1, several TDEs in the literature have exhibited double-peaked optical light curves. However, to our knowledge, with the exception of AT 2022cmc (I. Andreoni et al. 2022) no TDE has been reported to have an early component with distinct red colors like that seen in AT 2024kmq. To assess the prevalence of this phenomenon, we examined the light curves of the 44 TDEs detected by ZTF at z < 0.1 as part of the Bright Transient Survey³⁶ (BTS; C. Fremling et al. 2020; D. A. Perley et al. 2020). We selected this relatively small volume because at such nearby distances, the early component in AT 2024kmq—which $M < -19 \,\mathrm{mag}$ for ≈ 1 week—would be a full magnitude brighter than ZTF's typical limiting magnitude m = 20.5 mag. In addition, within this volume the ZTF BTS would be reasonably complete for TDEs with main peaks brighter than M = -20 mag. In AT 2024kmg, the fast red peak occurred \approx 40 days prior to the main peak.

We examined the 44 light curves starting from 40 days before peak. In some cases, the rise of the TDE light curve was not well sampled, or there was a long gap between the last nondetection and the first detection. However, in 21 cases an early peak of the same brightness and timescale can be ruled out. Even with $\gtrsim 1$ week long observing gaps, the fact that

none of the remaining 23 objects have such a component detected suggests that an early peak with these characteristics (luminosity, color, and timescale) is a rare phenomenon.

3.4. Optical Light Curve: Basic Properties

Figure 1 shows two distinct components in the optical light curve: an early fast and red component, and a slower blue component. We first consider the early red component. We fit a blackbody to the LDT gri imaging at $\Delta t \approx 1$ week (Figure 8) and find $L_{\rm BB} = 1.5^{+0.2}_{-0.2} \times 10^{43}$ erg s⁻¹, $T_{\rm BB} = 5.5^{+0.9}_{-1.2} \times 10^3$ K, and $R_{\rm BB} = 4.7^{+4.1}_{-1.0} \times 10^{15}$ cm. We caution that photometry in this region is challenging due to the brightness of the host galaxy—to account for this we add systematic uncertainties to the LDT measurements as described in Section 2.2—but the overall finding of red colors is robust.

Another possible emission mechanism for the first peak is synchrotron radiation. For synchrotron emission we can estimate the equipartition energy $U_{\rm eq}$ and magnetic field strength $B_{\rm eq}$. The latter is, from A. T. Moffet (1975),

$$B_{\rm eq} = \left(\frac{8\pi Ag(\beta)L}{V}\right)^{2/7},\tag{1}$$

where $A=1.586\times 10^{12}$ in cgs units, L is the luminosity, V is the volume of the synchrotron-emitting electrons, and $g(\beta)$ is a function of the spectral index β (defined as $f_{\nu} \propto \nu^{\beta}$) and frequency range (ν_1 to ν_2) for the power law:

$$g(\beta) = \frac{2\beta + 2}{2\beta + 1} \left[\frac{\nu_2^{\beta + 1/2} - \nu_1^{\beta + 1/2}}{\nu_2^{\beta + 1} - \nu_1^{\beta + 1}} \right]. \tag{2}$$

Using the peak optical brightness, adopting a spectral index from the gr observations of $f_{\nu} \propto \nu^{-2}$, and assuming the power law extends from 10^{13} Hz to 10^{15} Hz, we find $B_{\rm eq} \approx 10$ G, which is relatively insensitive to our choices of ν_1 , ν_2 , and α .

 $^{^{35}}$ In some other TDEs, power-law X-ray emission only appears at very late times when the system becomes sub-Eddington, but AT 2024kmq might be different. As discussed in Section 3.1, its black hole mass is likely large ($M_{\rm BH}\sim 10^8\,M_{\odot}$), so $L_{\rm X}\sim 10^{44}\,{\rm erg\,s^{-1}}$ is sub-Eddington by $\sim\!2$ orders of magnitude.

³⁶ We required the peak brightness to be m < 19 mag, and imposed a "quality cut" in the BTS Sample Explorer (D. A. Perley et al. 2020). The quality cut is based on the P48 coverage close to the peak of the light curve, and requires at least a \sim 1 week cadence.

Table 4 Best-fit Blackbody Parameters for the Optical and UV Light Curve of AT 2024kmq

Δt (days)	$L (10^{44} \text{ erg s}^{-1})$	T (10 ⁴ K)	R (10 ¹⁵ cm)
7 42 ^a 43 52 ^a 53 ^b 54 ^b 59 ^b 60 ^b 62	$0.15^{+0.02}_{-0.02}$ $4.6^{+3.4}_{-1.5}$ $2.9^{+0.8}_{-0.4}$ $1.7^{+0.2}_{-0.3}$ $6.0^{+0.6}_{-0.5}$ $6.1^{+0.2}_{-0.2}$ $5.2^{+0.2}_{-0.2}$ $5.0^{+0.2}_{-0.2}$	$\begin{array}{c} 0.54^{+0.09}_{-0.1} \\ 1.5^{+0.5}_{-0.3} \\ 1.2^{+0.1}_{-0.1} \\ 0.82^{+0.07}_{-0.10} \\ 1.7^{+0.2}_{-0.2} \\ 1.6^{+0.1}_{-0.1} \\ 1.7^{+0.1}_{-0.1} \\ 1.7^{+0.1}_{-0.1} \\ 1.4^{+0.2}_{-0.1} \end{array}$	$4.8_{-1.1}^{+3.6}$ $3.5_{-0.9}^{+0.8}$ $4.4_{-0.4}^{+0.6}$ $7.1_{-0.7}^{+1.3}$ $3.1_{-0.6}^{+0.6}$ $3.6_{-0.3}^{+0.5}$ $3.1_{-0.3}^{+0.4}$ $2.8_{-0.1}^{+0.1}$
69	$3.2_{-1.3}^{+0.9}$ $2.1_{-0.4}^{+0.6}$	$1.4_{-0.3}^{+0.2} \\ 1.3_{-0.1}^{+0.2}$	$3.4_{-0.6}^{+0.9}$ $3.4_{-0.4}^{+0.4}$

Notes. The first row corresponds to the early red peak and the remaining rows correspond to the slower blue component.

Next, we estimate the equipartition energy

$$U_{\rm eq} = 2\frac{VB^2}{8\pi} \tag{3}$$

and find $U_{\rm eq} \approx 6 \times 10^{47}\,{\rm erg}$. Finally, we consider the slower blue component, which is similar to that of optically discovered featureless TDEs. We construct an SED at each epoch of multiband LT and/or Swift/UVOT observations. To each SED epoch, we fit a blackbody using a Monte Carlo simulation with 600 trials (Figure 8), i.e., we resample the observed fluxes assuming a Gaussian distribution with a standard deviation equal to the measurement uncertainty. The resulting best-fit blackbody parameters are provided in Table 4. The blackbody temperatures of a few $\times 10^4$ K are similar to those of previously observed TDEs (E. Hammerstein et al. 2023; Y. Yao et al. 2023).

3.5. Radio Emission: Basic Properties

As discussed in Section 2.6, we detect luminous radio emission at the position of AT 2024kmq, but this radio source is likely dominated by an AGN. Radio AGN are known to occur preferentially in massive early-type galaxies (e.g., P. N. Best et al. 2005). From our LoTSS DR2 flux density measurement, we calculate a radio luminosity of $L_{150 \mathrm{MHz}} \approx 7 \times 10^{23} \mathrm{W Hz}^{-1}$ for the host of AT 2024kmg. According to J. Sabater et al. (2019), for galaxies of a similar mass, approximately 2% will be as luminous as the host of AT 2024kmq at 150 MHz. In addition, in galaxies as massive as the host of AT 2024kmq it is common for the AGN to lack detected optical emission lines (G. Kauffmann et al. 2008), consistent with our GMOS spectrum of the host galaxy of AT 2024kmq (Section 2.1). Also, radio-selected AGN tend not to be selected as optical or infrared AGN, and to have very low accretion rates (small Eddington ratios; R. C. Hickox et al. 2009).

The AGN origin can also explain the discrepancy between the AMI-LA 15.5 GHz measurements and our VLA 15 GHz observations. The AMI-LA beam is much larger than the VLA beam, and therefore is sensitive to extended emission, which

would result in a brighter source. Indeed, if we compare the LoTSS 150 MHz, RACS-Mid 1.4 GHz, and AMI-LA 15.5 GHz measurements, we will find that they trace a continuous radio spectrum with spectral index $\beta \approx -0.8$ (using the convention $f_{\nu} \propto \nu^{\beta}$, Figure 6), similar to the typical values for AGN (J. J. Condon et al. 2002; J. Sabater et al. 2019).

K. D. Alexander et al. (2020) define "radio-loud" TDEs as those that have $\nu L_{\nu} > 10^{40} \,\mathrm{erg \, s^{-1}}$, while the radio source coincident with AT 2024kmq is at $\approx 10^{39} \,\mathrm{erg \, s^{-1}}$. Any centimeter-wave radio counterpart of AT 2024kmq is at least 2 orders of magnitude less luminous than that of on-axis jetted TDEs at \approx 100 days. The observed spectral index of close to $F_{\nu} \propto \nu^{-1}$ (Figure 6) is similar to what was observed for the host galaxy of the TDE ASASSN-14li (K. D. Alexander et al. 2016).

4. Origin of the First Optical Peak

We consider two possible origins for the early red peak in the optical light curve: an off-axis jet (Section 4.1), and shocks from self-intersecting debris (Section 4.2).

4.1. Off-axis Jet Model

Our consideration of an off-axis jet model is motivated by the fact that the only other TDE with early fast red optical emission was AT 2022cmc, widely modeled as an on-axis jetted TDE (I. Andreoni et al. 2022; T. Matsumoto & B. D. Metzger 2023; D. R. Pasham et al. 2023; Y. Yao et al. 2024). The early fast red emission in AT 2024kmg is 2 orders of magnitude less luminous, so we consider the possibility that the jet was viewed off-axis. The effect of viewing the jet off-axis can be seen from the prescription developed for gamma-ray bursts (GRBs) in J. Granot et al. (2002), which assumes an emitting point source and accounts for the change in Doppler factor with the viewing angle. Specifically, for a viewing angle θ_{obs} we can calculate the factor

$$a(t) = \frac{1 - \beta(t)}{1 - \beta \cos \theta_{\text{obs}}}.$$
 (4)

Then, the off-axis light curve is

$$F_{\text{off}} = a^3 F_{\text{on},\nu/a}(at),\tag{5}$$

where F_{on} is calculated for a modified time a(t)t and frequency $\nu_{\rm obs}/a(t)$. For a jet with identical properties to those of AT 2022cmc, suppressing the optical emission by 2 orders of magnitude would require an off-axis parameter $a \approx 5$. Off-axis TDE afterglow light curves have previously been explored in the context of Swift J1644+57 (S. van Velzen et al. 2013; P. Mimica et al. 2015; A. Generozov et al. 2017; P. Beniamini et al. 2023).

To explore the jet model in more detail, we calculate the optical (g-band; 6×10^{14} Hz) and radio (10 GHz) light curves following the approach in T. Matsumoto & B. D. Metzger (2023) and T. Matsumoto & T. Piran (2021), which is based on standard GRB afterglow theory (R. Sari 1998; J. Granot & R. Sari 2002). Interpreting the early optical emission as synchrotron emission from a jet afterglow (instead of a blackbody as shown in Figure 8), we have a spectral index that is quite steep. The best-fit spectral index to the LDT gri epoch is $f_{\nu} \propto \nu^{-1.8 \pm 0.4}$, so electrons would likely be fast-cooling with

Observations impacted by poor seeing conditions.

^b Measurement includes Swift/UVOT photometry.

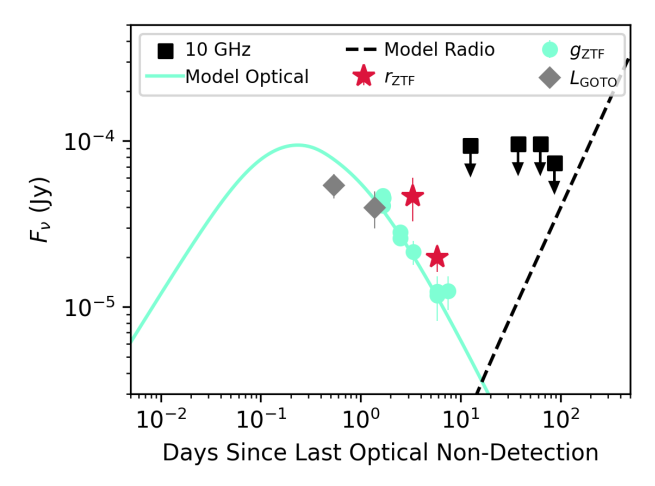


Figure 9. Model optical (*g*-band; solid line) and radio (10 GHz; dashed line) light curves for an off-axis jet. Optical observations are plotted as circles (*g*-band), diamonds (*L*-band), and stars (*r*-band), while upper limits from the 10 GHz radio observations (assuming detections are from the host galaxy) are plotted as squares.

 $p \approx 3$. As argued in T. Matsumoto & B. D. Metzger (2023), the fact that the electrons are fast-cooling disfavors a reverse shock origin for the early optical flare, as this would predict a more abrupt decline in the early peak than what we observe. So, we assume that the early optical emission arises from a decelerating forward shock.

Details and assumptions of the model are provided in Appendix B. Figure 9 shows the optical and radio data along with an off-axis jet model with the following physical parameters: microphysical parameters $\epsilon_B = 0.002$ and $\epsilon_e = 0.2$; jet energy $E_{52} = 5$; jet initial Lorentz factor $\Gamma_0 = 3$; density $n_{17} = 20,000 \, \mathrm{cm}^{-3}$, where $n = n_{17} (R/10^{17} \, \mathrm{cm})^{-k}$ and k = 1; jet opening angle $\theta_j = 0.1$; power-law index for the particle energy distribution p = 2.2; and observing angle from the jet axis $\theta_{\mathrm{obs}} = 0.4$.

As shown in Figure 9, the off-axis jet model provides a reasonable description of the rapid early optical evolution, as well as the late-time radio nondetections. However, the model underpredicts the observed X-ray luminosity by 2 orders of magnitude, consistent with previous work on jetted TDEs that attributes the hard variable X-rays to emission internal to the jet rather than to the forward shock (J. S. Bloom et al. 2011; B. A. Zauderer et al. 2011; P. Crumley et al. 2016; T. Matsumoto & B. D. Metzger 2023; Y. Yao et al. 2024), or alternatively to an external reverse shock (C. Yuan et al. 2025).

In this model, the early optical emission is suppressed by the fact that the jet is observed off-axis: the off-axis parameter a varies from a=0.5 at $\Delta t=0.1$ days to a=0.9 at $\Delta t=10$ days. If this jet were viewed on-axis, the peak optical luminosity would be an order of magnitude fainter than that of AT 2022cmc, primarily because the jet energy is an order of magnitude smaller. The viewing angle does not significantly suppress the radio luminosity; by our last radio observation, the shock is almost Newtonian. The radio peak is suppressed until late times by synchrotron self-absorption, so the timing of the radio peak is essentially set by the circumnuclear density. We note that a circumnuclear density of $20,000\,\mathrm{cm}^{-3}$ at $10^{17}\,\mathrm{cm}$ (or $1000\,R_s$ for a Schwarzschild radius of $R_s=10^{14}\,\mathrm{cm}$, as expected for a $4\times10^8\,M_\odot$ black hole) is similar to that inferred for the TDE AT 2019dsg (K. D. Alexander et al. 2020; Y. Cendes et al. 2021). Testing this model

requires late-time radio observations to search for the predicted brightening in the radio light curve.

4.2. Shocks from Self-intersecting Debris

The black hole in AT 2024kmq is likely quite massive, with mass $M \approx 10^8 \, M_\odot$ (Section 3.1), such that the tidal radius $r_t = R_\star (M/M_\star)^{1/3}$ is a few gravitational radii for a Sun-like star. Apsidal precession then amounts to many tens of degrees and circularization is likely efficient (M. J. Rees 1988). In particular, the incoming and outgoing streams collide at large angles, producing two shocks and a contact discontinuity separating the two unshocked fluids. After approximately the freefall time from the self-intersection radius, the incoming debris stream must be replenished to initiate a second, strong self-intersection, and this process repeats until the disk of material (generated by prior intersections and viscous accretion) is sufficiently dense that the incoming stream disintegrates via the Kelvin–Helmholtz instability and the system settles into more of a steady state (Z. L. Andalman et al. 2022).

The primary effect of the prompt self-intersection shocks will be to thermalize the gas to a pressure of $p \simeq \rho v^2$, where ρ is the density and $v \simeq$ a few $\times 0.1c$ is the velocity of the stream at the self-intersection point for these highly relativistic encounters. The shocked material then expands at approximately the original speed within the plane and the sound speed in the plane perpendicular to fill a quasi-spherical volume, up to $\sim 10\%$ of which may be unbound from the black hole³ (Y.-F. Jiang et al. 2016; X. Huang et al. 2023, 2024; see also C. Bonnerot et al. 2021 for analytical estimates). It thus seems possible that some debris is ejected on positive-energy orbits at speeds comparable to the speed at which gas self-intersects, $\sim 0.1c$ (in this case). Irrespective of its boundedness, a substantial amount of the debris recedes to distances comparable to the initial apocenter distance as set during the initial disruption process, which is $R_{\star}(M/M_{\star})^{2/3} \simeq 10^{16} M_8^{2/3}$ cm (J. H. Lacy et al. 1982).

The returning stream can be crudely approximated as a cylinder with cross-sectional radius R_{\star} and length equal to the apocenter of the most-bound debris (T. Wevers et al. 2023), which yields $\rho \simeq \rho_0 M_8^{-2/3}$ with $\rho_0 \simeq 10^{-8} - 10^{-10}$ g cm⁻³. The shocked gas is highly optically thick and radiation pressure dominated, such that the jump conditions relate the ram pressure to the temperature T via $\rho v^2 \simeq a T^4/3$, which gives (with $\rho_0 = 10^{-9}$ g cm⁻³ and $v \sim$ a few \times 0.1c) $T = 1.4 \times 10^6 M_8^{-1/6}$ K; this agrees with the temperatures inferred by Y.-F. Jiang et al. (2016).

The shock-heated debris expands quasi-spherically, and if its velocity profile is approximately homologous, the temperature of the (radiation pressure dominated and optically thick) gas declines with the leading edge of the expanding cloud R as $T \propto R^{-1}$. If the stream collision occurs at $5GM/c^2$ and has an initial temperature of 10^6 K, then by the time the cloud expands to the apocenter of the most-bound debris, the temperature decreases to $\sim 5 \times 10^3 M_8^{1/6}$ K. If the bulk of the emission originates near the edge of the cloud and the material is only marginally bound, the luminosity declines with time

³⁷ There are caveats with this interpretation, e.g., Y.-F. Jiang et al. (2016) did not include the gravitational field of the black hole, and X. Huang et al. (2023) represented boundedness through an instantaneous Bernoulli-like parameter, the positivity of which does not guarantee successful ejection for time-dependent flows; see E. R. Coughlin et al. (2018) for a specific case.

as³⁸ $L \propto R^2 T^4 \propto t^{-4/3}$, with a value of $L \simeq 9 \times 10^{43} M_8^2$ erg s⁻¹ near the debris apocenter (note that this strong black hole mass dependence only enters for relativistic encounters where $v \simeq 0.1c$ at self-intersection).

This temperature near the apocenter and the value and temporal decline of the luminosity are roughly consistent with the early and red outburst from AT 2024kmq. While this temperature is lower than the values of about a few \times 10⁴ K that are inferred from radiation-hydrodynamical simulations (Y.-F. Jiang et al. 2016), the time taken for the debris to reach the apocenter distance of \sim 10¹⁵ cm is \lesssim 1 day if it is moving at 0.3c, and the earlier and hotter phases of the evolution could have been missed.

If the early red outburst was due to the expanding cloud of debris produced from the initial stream self-intersection, it is natural to associate the second, larger and bluer outburst with fallback accretion onto the black hole. However, the time taken to reach the peak in the fallback rate is (A. Bandopadhyay et al. 2024) $\sim 20 \times (M/10^6 M_{\odot})^{1/2} \simeq 200$ days for $M=10^8~M_{\odot}$, which is a factor of $\sim 5~longer^{39}$ than the $\sim 40~longer^{39}$ days observed (see Figure 1). It has been argued that the rise in the fallback rate is steeper for partial TDEs (C. J. Nixon et al. 2021), and a partial TDE is more likely for such a massive black hole. However, the luminosity of this second blue peak is fairly typical for TDEs, so we have no evidence that the star was only partially stripped.

Another challenge for the self-intersection model is that this mechanism is thought to be ubiquitous in TDEs, facilitating the circularization of the debris and subsequent accretion onto the black hole (M. J. Rees 1988). So, a natural question to ask is why outbursts with similar properties are uncommon (Section 3.3). One possibility is that most TDEs are powered by lower-mass black holes, for which self-intersection occurs far less violently and at much larger (nonrelativistic) radii. 40 Specifically, in the limit that the relativistic apsidal precession angle is small and given by the leading-order, relativistic value of $\delta \phi = 3GM/(r_t c^2)$ (e.g., S. M. Carroll 2004), the self-intersection radius is $r_{\rm SI} \simeq 2r_t/\delta\phi$, leading to a velocity at the point of self-intersection of $v_{\rm SI} \simeq \sqrt{GM/r_{\rm SI}} \simeq c \times (GM/(r_{\rm t}c^2))$. The radiation pressure resulting from the shock is then $p_{\rm rad} \simeq aT^4 \simeq \rho c^2 (GM/(r_t c^2))^2$, which is reduced by a factor of $(GM/(r_tc^2))^2$ relative to the relativistic value discussed in the preceding paragraphs; for $M=10^6~M_{\odot}$ and a solar-like star, this factor is $\sim 4 \times 10^{-4}$, such that the dissipation is far less efficient at powering a luminous outburst. It also seems likely that more material remains bound to the black hole (or at least material is ejected with a much smaller speed) following

a comparatively less violent self-intersection, implying that most of the radiation is trapped within the flow that falls back to smaller radii, where the process of accretion can liberate substantially more energy.

5. Summary

We have presented the identification of AT 2024kmq as a fast, red, and luminous optical transient, and its subsequent classification as a TDE by a massive (likely $M \approx 10^8 M_{\odot}$) black hole. With follow-up UV, optical, X-ray, and radio observations, we detected luminous and variable hard X-rays ($10^{44}\,\mathrm{erg\,s^{-1}}$) and featureless optical spectra and set a limit on the presence of a radio counterpart ($L < 10^{39}\,\mathrm{erg\,s^{-1}}$ at 10 GHz from $\Delta t = 10$ –100 days). The radio emission detected at the transient position is likely from an underlying AGN; radio AGN are common in galaxies of this type.

To our knowledge, an early optical peak with distinctly red colors in a TDE has only been seen in AT 2022cmc, which is widely modeled as an on-axis jetted TDE. Using nearby TDEs classified as part of ZTF's flux-limited experiment, we find that early peaks with a similar luminosity and duration (M < -19 mag for 1 week) are uncommon.

We consider two possibilities for the origin of the early red peak: an off-axis jet, and self-intersecting debris streams leading to the formation of the accretion disk. The off-axis jet model is motivated by AT 2022cmc and the suggestion in the literature that "featureless TDEs" are associated with jets. For a jet, we find that an off-axis viewing angle ($\theta_{\rm obs} = 0.4$, which is $4\times$ the jet opening angle) and a low jet energy ($E_j = 5\times 10^{52}$ erg, an order of magnitude lower than that of AT 2022cmc) are required to suppress the luminosity of the optical peak relative to what was observed in AT 2022cmc. In addition, a circumnuclear density of $n_{17} = 20,000 \, {\rm cm}^{-3}$ is required to suppress the radio emission until late times. Under this model, the radio emission should eventually be detectable, on timescales of years.

For the self-intersecting debris stream model, we find that the highly relativistic nature of the encounter (due to the high mass of the black hole) could produce optical emission with a similar temperature and luminosity. In this model, it is natural to explain the second blue peak as fallback accretion onto the black hole, although the timescale is challenging to explain. The fact that such luminous optical flares are relatively uncommon could be because they are much fainter in encounters involving lower-mass black holes.

The code used to perform the calculations and produce the figures for this paper is available in a public Zenodo repository⁴¹ via doi:10.5281/zenodo.15650390.

Acknowledgments

A.Y.Q.H. would like to thank Eliot Quataert, Dong Lai, and Wenbin Lu for helpful conversations regarding TDE models as well as Krista Lynne Smith for discussions about radio AGN. Eric R. Coughlin acknowledges support from NASA through the Astrophysics Theory Program, grant 80NSSC24K0897. J.D.L. acknowledges support from a UK Research and Innovation Future Leaders Fellowship (MR/T020784/1). I.A. is supported by NSF AST2407924 and NASA ADAP24-0159.

 $^{^{38}}$ This temporal scaling assumes that the debris is still in the phase where it is moving out on a zero-energy orbit, i.e., $0.5(dR/dt)^2 \sim GM/R$; this is justified from the fact that a few \times 10^{15} cm is still less than the apocenter distance of $\sim 10^{16}$ cm. If one instead assumes that the surface has reached the phase where it moves at a constant velocity, then the luminosity declines with time as $L \propto t^{-2}$.

³⁹ Note that this timescale is insensitive to the stellar properties, which agrees with numerical results (J. Guillochon & E. Ramirez-Ruiz 2013; T. Jankovič & A. Gomboc 2023) and analytical predictions (E. R. Coughlin & C. J. Nixon 2022), hence invoking, e.g., that a more massive star does not alleviate this tension. Similarly, relativistic effects do not strongly impact the fallback time, even when the pericenter is highly relativistic (e.g., E. Gafton & S. Rosswog 2019).

⁴⁰ Another possibility is that the spin of the black hole and Lense–Thirring (nodal) precession results in no initial collision (J. Guillochon et al. 2016), with self-intersection happening later and at a time when the density would have fallen by a much larger factor; qualitatively similar conclusions are reached when considering this possibility.

⁴¹ The code is also available in a public GitHub repository: https://github.com/annayqho/AT2024kmq.

C.L. is supported by DoE award #DE-SC0025599. J.S. is supported by NASA award 80NSSC24K0377.

This work was performed in part at the Aspen Center for Physics, which is supported by National Science Foundation grant PHY-2210452.

Based on observations obtained with the Samuel Oschin telescope 48 inch and the 60 inch telescope at the Palomar Observatory as part of the ZTF project. ZTF is supported by the National Science Foundation under grant No. AST-2034437 and a collaboration including Caltech, IPAC, the Oskar Klein Centre at Stockholm University, the University of Maryland, University of California, Berkeley, the University of Wisconsin at Milwaukee, University of Warwick, Ruhr University Bochum, Cornell University, Northwestern University, and Drexel University. Operations are conducted by COO, IPAC, and UW. The ZTF forced-photometry service was funded under Heising-Simons Foundation grant No. 12540303 (PI: Graham). The Gordon and Betty Moore Foundation, through both the Data-driven Investigator Program and a dedicated grant, provided critical funding for SkyPortal.

SEDM is based on work supported by the National Science Foundation under grant No. 1106171. Data were obtained at the Lick Observatory, which is a multicampus research unit of the University of California. Some of the data presented herein were obtained at the W. M. Keck Observatory, which is operated as a scientific partnership among the California Institute of Technology, the University of California, and NASA. The Observatory was made possible by the generous financial support of the W. M. Keck Foundation. The authors wish to recognize and acknowledge the very significant cultural role and reverence that the summit of Maunakea has always had within the indigenous Hawaiian community. We are most fortunate to have the opportunity to conduct observations from this mountain.

Based on observations carried out with the IRAM interferometer NOEMA. IRAM is supported by INSU/CNRS (France), MPG (Germany), and IGN (Spain).

This work made use of data supplied by the UK Swift Science Data Centre at the University of Leicester.

This work uses data obtained with the eROSITA telescope on board the SRG observatory. The SRG observatory was built by Roskosmos with the participation of the Deutsches Zentrum für Luft- und Raumfahrt (DLR). The SRG/eROSITA X-ray telescope was built by a consortium of German institutes led by MPE, and supported by DLR. The SRG spacecraft was designed, built, and launched and is operated by the Lavochkin Association and its subcontractors. The science data were downlinked via the Deep Space Network Antennae in Bear Lakes, Ussurijsk, and Baykonur, funded by Roskosmos. The eROSITA data used in this work were processed using the eSASS software system developed by the German eROSITA Consortium and proprietary data reduction and analysis software developed by the Russian eROSITA Consortium.

The National Radio Astronomy Observatory is a facility of the National Science Foundation operated under a cooperative agreement by Associated Universities, Inc. LOFAR is the Low-frequency Array designed and constructed by ASTRON. It has observing, data processing, and data storage facilities in several countries, which are owned by various parties (each with its own funding sources), and which are collectively operated by the International LOFAR Telescope (ILT) foundation under a joint scientific policy. The ILT resources have benefited from the following recent major funding sources: CNRS-INSU, Observatoire de Paris, and Université d'Orléans, France; BMBF, MIWF-NRW, and MPG, Germany; Science Foundation Ireland and Department of Business, Enterprise and Innovation (DBEI), Ireland; NWO, the Netherlands; the Science and Technology Facilities Council, UK; Ministry of Science and Higher Education, Poland; and the Istituto Nazionale di Astrofisica (INAF), Italy.

This research made use of the Dutch national e-infrastructure with support of the SURF Cooperative (e-infra 180169) and the LOFAR e-infra group. The Jülich LOFAR Long Term Archive and the German LOFAR network are both coordinated and operated by the Jülich Supercomputing Centre (JSC), and computing resources on the supercomputer JUWELS at JSC were provided by the Gauss Centre for Supercomputing e.V. (grant CHTB00) through the John von Neumann Institute for Computing.

This research made use of the University of Hertfordshire high-performance computing facility and the LOFAR-UK computing facility located at the University of Hertfordshire and supported by STFC [ST/P000096/1], and of the Italian LOFAR IT computing infrastructure supported and operated by INAF, and by the Physics Department of Turin University (under an agreement with Consorzio Interuniversitario per la Fisica Spaziale) at the C3S Supercomputing Centre, Italy.

This scientific work uses data obtained from Inyarrimanha Ilgari Bundara, the CSIRO Murchison Radio-astronomy Observatory. We acknowledge the Wajarri Yamaji people as the traditional owners and native title holders of the Observatory's site. CSIRO's ASKAP radio telescope is part of the Australia Telescope National Facility (https://ror.org/05qajvd42). Operation of ASKAP is funded by the Australian Government with support from the National Collaborative Research Infrastructure Strategy. ASKAP uses the resources of the Pawsey Supercomputing Research Centre. ASKAP, Inyarrimanha Ilgari Bundara, the CSIRO Murchison Radio-astronomy Observatory, and the Pawsey Supercomputing Research Centre are initiatives of the Australian Government, with support from the Government of Western Australia and the Science and Industry Endowment Fund.

This paper includes archived data obtained through the CSIRO ASKAP Science Data Archive, CASDA (http://data.csiro.au).

Facilities: PO:1.2m, Keck:I, Shane, Swift, EVLA, LDT, Liverpool:2m.

Software: CASA (J. P. McMullin et al. 2007), Astropy (Astropy Collaboration et al. 2013, 2018, 2022).

Appendix A Additional Data Tables

We present the optical photometry in Table 5 and the radio observations in Table 6.

60503.20007

60504.32406

42.96

44.08

ZTF/P48

ATLAS

g o

17.99

18.25

Table 5 Optical Photometry of AT 2024kmq

Table 5 (Continued)

Optical Photometry of AT 2024kmq					(Continued)						
Start MJD	$\Delta t_{ m obs}$ (days)	Instrument	Filter	Mag ^a	eMag	Start MJD	$\Delta t_{ m obs}$ (days)	Instrument	Filter	Mag ^a	eMag
60460.88621	0.64	GOTO	L	19.63	0.19	60505.19919	44.95	ZTF/P48	g	17.96	0.04
60461.88658	1.64	GOTO	L	19.97	0.27	60505.21012	44.97	P60/SEDM	g	18.08	0.04
60462.22313	1.98	ZTF/P48 ^b	g	19.95	0.08	60505.21281	44.97	P60/SEDM	r	18.19	0.04
60462.22406	1.98	ZTF/P48	g	19.80	0.08	60505.21550	44.97	P60/SEDM	i	18.44	0.06
60462.25939	2.01	ZTF/P48 ATLAS	g	19.83	0.07 0.22	60505.29805	45.05	ATLAS	0	18.35	0.09
60462.35100 60463.19822	2.11 2.95	ZTF/P48	0	19.65 20.35	0.22	60506.31464	46.07	ATLAS	0	18.39	0.12
60463.21853	2.93	ZTF/P48 ZTF/P48	g	20.33	0.12	60506.90029	46.66	GOTO	L	18.27	0.22
60463.31845	3.07	ATLAS	g 0	20.08	0.19	60507.28860	47.04	ATLAS	0	18.33	0.08
60464.21958	3.97	ZTF/P48	r	19.79	0.32	60508.29117	48.05	ATLAS	0	18.53	0.09
60464.23774	3.99	ZTF/P48	g	20.65	0.18	60509.20082 60509.27089	48.96 49.03	ZTF/P48 ATLAS	g	18.08 18.40	0.06 0.10
60467.21535	6.97	LDT/LMI	r	20.70	0.20	60510.19566	49.03	ZTF/P48	0	18.40	0.10
60467.21888	6.97	P60/SEDM	g	21.25	0.13	60510.31427	50.07	ATLAS	g 0	18.39	0.10
60467.22667	6.98	LDT/LMI	i	20.50	0.12	60510.52183	50.28	Swift/UVOT	UVM2	18.15	0.10
60467.23357	6.99	LDT/LMI	g	21.30	0.32	60511.30985	51.06	ATLAS	0	18.64	0.16
60467.28723	7.04	ATLAS	o	20.42	0.34	60511.90682	51.66	LT/IO:O	g	18.19	0.10
60469.18617	8.94	ZTF/P48	g	21.24	0.25	60511.90783	51.66	LT/IO:O	i	18.72	0.08
60479.21865	18.97	ZTF/P48	g	20.61	0.32	60511.90885	51.66	LT/IO:O	r	18.30	0.12
60480.20184	19.96	ZTF/P48	g	20.50	0.30	60511.90984	51.66	LT/IO:O	z	18.38	0.15
60480.23791	19.99	ZTF/P48	g	20.45	0.34	60512.90387	52.66	Swift/UVOT	UVW1	17.76	0.06
60481.19624	20.95	ZTF/P48	g	20.45	0.26	60512.90530	52.66	Swift/UVOT	U	17.73	0.07
60481.26595	21.02	ZTF/P48	g	20.19	0.36	60512.90628	52.66	Swift/UVOT	B	17.96	0.14
60482.21664	21.97	ZTF/P48	g	20.31	0.30	60512.90866	52.66	Swift/UVOT	UVW2	18.01	0.05
60483.19494	22.95	ZTF/P48	g	19.81	0.19	60512.91102	52.67	Swift/UVOT	V	18.33	0.33
60483.24196	23.00	ZTF/P48	g	20.07	0.29	60512.91262	52.67	Swift/UVOT	UVM2	17.88	0.06
60484.26888	24.02	ZTF/P48	g	19.41	0.19	60514.29705	54.05	ATLAS	o	18.16	0.11
60485.30989	25.06	ATLAS	0	20.12	0.29	60514.65172	54.41	Swift/UVOT	UVW1	17.73	0.07
60486.20213	25.96	ZTF/P48	g	19.44	0.06	60514.65262	54.41	Swift/UVOT	U	17.62	0.08
60486.31891	26.07	ATLAS	0	19.73	0.21	60514.65369	54.41	Swift/UVOT	UVW2	18.07	0.06
60487.30585	27.06	ATLAS	0	19.68	0.17	60514.68398	54.44	Swift/UVOT	UVM2	17.92	0.06
60488.35730	28.11	ATLAS	o	19.41	0.16	60515.29560	55.05	ATLAS	o	18.50	0.08
60489.22517	28.98	ZTF/P48	g	18.88	0.05	60518.29390	58.05	ATLAS	o	18.49	0.09
60489.29718	29.05	ATLAS GOTO	0	19.09 19.07	0.11	60518.92244	58.68	Swift/UVOT	UVM2	18.10	0.08
60490.96002 60492.30819	30.72 32.06	ATLAS	L = o	19.07	0.12 0.10	60518.92483	58.68	Swift/UVOT	UVW1	17.88	0.08
60492.91381	32.67	GOTO	L L	18.79	0.10	60518.92629	58.68	Swift/UVOT	U	17.86	0.10
60494.29771	34.05	ATLAS	0	18.79	0.10	60518.92835	58.68	Swift/UVOT	UVW2	18.26	0.07
60495.29996	35.06	ATLAS	0	18.70	0.10	60519.18373	58.94	ZTF/P48	g	18.17	0.04
60495.89886	35.65	GOTO	L	18.58	0.10	60519.19725	58.95	ZTF/P48	g	18.35	0.07
60497.26798	37.02	ATLAS	0	18.67	0.08	60519.90265	59.66	LT/IO:O	8	18.24	0.10
60498.31610	38.07	ATLAS	0	18.56	0.07	60519.90493	59.66	LT/IO:O	i	18.96	0.09
60499.19725	38.95	ZTF/P48	g	18.11	0.03	60519.90734	59.66	LT/IO:O	r	18.45	0.04
60499.89569	39.65	GOTO	$\stackrel{\circ}{L}$	18.15	0.08	60519.90961	59.66	LT/IO:O	Z 1.11.11.10	18.71	0.14
60500.20609	39.96	ZTF/P48	g	18.10	0.03	60520.23891 60520.24083	59.99 60.00	Swift/UVOT Swift/UVOT	UVM2 UVW1	18.15 17.95	0.07 0.07
60500.22086	39.98	ZTF/P48	g	18.08	0.04	60520.24202	60.00	Swift/UVOT	U	17.93	0.07
60501.20279	40.96	ZTF/P48	g	17.98	0.03	60520.24340	60.00	Swift/UVOT	UVW2	18.28	0.06
60501.21436	40.97	ZTF/P48	g	17.98	0.03	60521.17615	60.93	P60/SEDM	r	18.40	0.05
60501.89200	41.65	GOTO	L	18.40	0.09	60521.17885	60.93	P60/SEDM	i	18.45	0.05
60501.93506	41.69	LT/IO:O	g	18.15	0.17	60521.89335	61.65	LT/IO:O	g	18.33	0.03
60501.93629	41.69	LT/IO:O	r	18.29	0.09	60521.89629	61.65	LT/IO:O	s r	18.42	0.03
60501.93749	41.69	LT/IO:O	i	18.74	0.09	60521.89739	61.65	LT/IO:O	i	18.71	0.10
60501.93870	41.69	LT/IO:O	z	18.17	0.13	60521.89952	61.65	LT/IO:O	z.	18.85	0.10
60501.93996	41.70	LT/IO:O	и	17.80	0.22	60528.88471	68.64	LT/IO:O	g	18.60	0.10
60502.20354	41.96	ZTF/P48	g	18.06	0.04	60528.88572	68.64	LT/IO:O	r	18.53	0.05
60502.23672	41.99	P60/SEDM	g	18.05	0.06	60528.88784	68.64	LT/IO:O	i	19.01	0.07
60502.23940	41.99	P60/SEDM	<i>r</i>	18.29	0.06	60528.88998	68.65	LT/IO:O	z.	19.24	0.11
60502.24210	42.00	P60/SEDM	i	18.42	0.03	60535.15262	74.91	ZTF/P48	r	18.65	0.11
60502.95101	42.71	LT/IO:O	r	18.32	0.07	60536.15222	75.91	ZTF/P48	r	18.66	0.11
60502.95316	42.71	LT/IO:O	<i>g</i>	18.13	0.18	60537.15089	76.91	ZTF/P48	r	19.42	0.24
60502.95509	42.71	LT/IO:O	i	18.51	0.09	60538.14762	77.90	ZTF/P48	r	18.89	0.18
60502.95722	42.71	LT/IO:O	z	18.75	0.15	60538.14855	77.90	ZTF/P48	r	19.09	0.20
60502.95941	42.71	LT/IO:O	и	17.99	0.20	60549.13608	88.89	ZTF/P48	r	18.87	0.30
60503.18232	42.94	P60/SEDM	g	18.15	0.06						
60503.18500	42.94	P60/SEDM	r	18.21	0.04	Notes.					
60503.18559	42.94 42.94	ZTF/P48 P60/SEDM	g ;	18.06	0.04		for Milky	Way extinction.			
60503.18770 60503.20007	42.94 42.96	7TF/P48	i	18.54 17.99	0.04	b From forced	photometry	on ZTF images.			

(This table is available in machine-readable form in the online article.)

0.05

0.06

^b From forced photometry on ZTF images.

Table 6VLA Observations of AT 2024kmq^b

Start MJD	$\Delta t_{ m obs}$ (days)	ν _{obs} (GHz)	Beam Size (arcsec)	Beam Angle (deg)	f_{ν} (Point Source) ^a (mJy)
60475.98	15.09	10	0.66×0.56	-64.31	0.112 ± 0.01
60505.82	44.93	6	1.34×1.06	81.57	0.191 ± 0.011
		10	0.73×0.56	88.88	0.114 ± 0.012
		15	0.54×0.39	-71.89	0.095 ± 0.011
60536.08	75.19	6	1.55×0.94	-75.48	0.172 ± 0.014
		10	0.93×0.57	-75.53	0.114 ± 0.013
60565.03	104.14	6	1.93×0.93	-70.36	0.152 ± 0.017
		10	1.16×0.62	-66.09	0.088 ± 0.013
		15	0.91×0.39	-68.0	0.048 ± 0.01

Notes

Appendix B Off-axis Jet Model

We assume a top-hat jet expanding into a medium with a density profile

$$n = n_0 (R/10^{17} \text{ cm})^{-k}$$
. (B1)

Assuming that the jet keeps its initial opening angle and neglecting the energy lost to radiation, energy conservation gives

$$E_{k \text{ iso}} = [M_{i \text{ iso}} + M_{\text{swent}}(R)\Gamma](\Gamma - 1)c^2$$
 (B2)

where

$$M_{\text{swept}}(R) \equiv \int_0^R 4\pi m_p n(r) r^2 dr$$
 (B3)

and $M_{j,\rm iso} \equiv E_{k,\rm iso}/(\Gamma_0-1)c^2$ is the jet's isotropic-equivalent original mass. To an observer, the jet radius evolves according to

$$\frac{dR}{dt} = \frac{\beta(R)c}{1 - \beta(R)} \tag{B4}$$

where β is the jet velocity, time t is the observer time and the denominator accounts for relativistic effects. We start the integration at a sufficiently short timescale that the jet may be regarded as freely expanding: $R_0 = (\beta_0 c) t_0 / (1 - \beta_0)$.

Once we solve for the dynamics, i.e., the evolution of the blastwave Lorentz factor $\Gamma(t)$, we calculate the light curve as follows. The magnetic field is given by

$$B = \sqrt{32\pi\epsilon_B m_p c^2 (\Gamma - 1)\Gamma}.$$
 (B5)

The characteristic and fast-cooling electron Lorentz factors are given by

$$\gamma_m = \max \left[2, \frac{m_p}{4m_e} \bar{\epsilon_e} (\Gamma - 1) \right]$$
 (B6)

and

$$\gamma_c = \frac{6\pi m_e c}{\sigma_{\rm T} B^2 \delta_{\rm D} t},\tag{B7}$$

where $\bar{\epsilon_e} = 4\epsilon_e \left(\frac{p-2}{p-1}\right)$ and $\delta_D = \frac{1}{\Gamma(1-\beta)}$. For a given Lorentz factor γ the corresponding synchrotron frequency is given by

$$\nu_{\rm syn}(\gamma) = \delta_{\rm D} \frac{eB\gamma^2}{2\pi m_e c}.$$
 (B8)

Since the synchrotron emissivity of a single electron with γ_m is given by

$$P_{\nu_m} = \delta_{\rm D} \Gamma \left[\frac{4}{3} \sigma_{\rm T} c \gamma_m^2 \frac{B^2}{8\pi} \right] \frac{1}{\nu_m},\tag{B9}$$

the flux at the frequency at which the bulk of electrons are emitting (ν_m in the slow-cooling regime, ν_c in the fast-cooling regime) is

$$F_{\nu_m} = N_e \frac{P_{\nu_m}}{4\pi d_r^2} \min[(\Gamma \theta_j)^2, 1],$$
 (B10)

and the number of electrons at that characteristic frequency is

$$N_e = \frac{M_{\text{swept}}(R)}{m_p} \min \left[1, \left(\frac{\beta}{\beta_{\text{DN}}} \right)^2 \right]$$
 (B11)

where the last factor in N_e is needed to take into account the deep Newtonian regime. Finally

$$\beta_{\rm DN} = \sqrt{\frac{16m_e}{\bar{\epsilon}_e m_p}} \tag{B12}$$

is the critical velocity below which $\gamma_m < 2$ in Equation (B6) and the deep Newtonian regime sets in.

To calculate the spectrum neglecting synchrotron self-absorption, we follow the prescription of J. Granot & R. Sari (2002). More specifically, for the slow-cooling regime of $\nu_m < \nu_c$ we use $F_{\nu} \propto \nu^{1/3}$ for $\nu < \nu_m$, $F_{\nu} \propto \nu^{-(p-1)/2}$ for $\nu_m < \nu < \nu_c$, and $F_{\nu} \propto \nu^{-p/2}$ for $\nu > \nu_c$. For the fast-cooling regime of $\nu_m > \nu_c$, we use $F_{\nu} \propto \nu^{1/3}$ for $\nu < \nu_c$, $F_{\nu} \propto \nu^{-1/2}$ for $\nu_c < \nu < \nu_m$, and $F_{\nu} \propto \nu^{-p/2}$ for $\nu_c < \nu_c$. To connect the power-law segments, following J. Granot & R. Sari (2002) we adopt a sharpness parameter s (with the value obtained from their Table 2). In addition, to smoothly connect the fast- and slow-cooling regimes, we calculate F_{ν} for both cases and take

 $^{^{}a}f_{\nu}$ is measured using imtool, which allows for a forced point-source fitting. When left to freely fit the shape, there are a few epochs where imtool prefers an extended shape; however for consistency we only quote the measured f_{ν} from the forced point-source fitting, which is not significantly different from the measured f_{ν} when an extended shape is preferred.

b The emission likely arises from the host galaxy, given that the flux density values do not change significantly over the course of our observations.

a weighted average:

$$F_{\nu} = \frac{\left(\frac{\nu_{c}}{\nu_{m}}\right)^{2} F_{\nu}^{\text{slow}} + \left(\frac{\nu_{m}}{\nu_{c}}\right)^{2} F_{\nu}^{\text{fast}}}{\left(\frac{\nu_{c}}{\nu_{m}}\right)^{2} + \left(\frac{\nu_{m}}{\nu_{c}}\right)^{2}}.$$
 (B13)

Next, we account for synchrotron self-absorption. The absorption coefficient is (G. B. Rybicki & A. P. Lightman 1986)

$$\alpha_{\nu} = \frac{\bar{p}\sqrt{3}e^{3}n\min\left[1,\left(\frac{\beta}{\beta_{\rm DN}}\right)^{2}\right]B\Gamma\delta_{\rm D}}{4\pi m_{e}^{2}c^{2}\gamma_{m}\nu^{2}}\left(\frac{\nu}{\nu_{m}}\right)^{-p/2}I(\nu), \quad (B14)$$

where $\bar{p} = (p+2)(p-1)$ and $I(\nu)$ is the integral:

$$I(\nu) = \int_0^{\nu/\nu_m} dx x^{\frac{p}{2}} \int_{x}^{\infty} dy K_{5/3}(y).$$
 (B15)

Alternatively, in terms of the synchrotron function F(x),

$$I(\nu) = \int_0^{\nu/\nu_m} dx x^{\frac{p-2}{2}} F(x).$$
 (B16)

We approximate F(x) using the fitting function in M. Fouka & S. Ouichaoui (2013). For $\nu/\nu_m \ge 10^4$, we use the following approximation for $I(\nu)$ from G. B. Rybicki & A. P. Lightman (1986):

$$I(\nu) = \frac{2^{\mu+1}}{\mu+2} \Gamma\left(\frac{\mu}{2} + \frac{7}{3}\right) \Gamma\left(\frac{\mu}{2} + \frac{2}{3}\right)$$
 (B17)

where in this case $\mu = (p-2)/2$. We multiply the light curve

$$\frac{1 - e^{-\tau}}{\tau} \tag{B18}$$

where $\tau = \alpha_{\nu} R$.

ORCID iDs

Anna Y. Q. Ho https://orcid.org/0000-0002-9017-3567 Yuhan Yao https://orcid.org/0000-0001-6747-8509 Tatsuya Matsumoto https://orcid.org/0000-0002-3809-0000

Genevieve Schroeder https://orcid.org/0000-0001-9915-8147

Eric R. Coughlin https://orcid.org/0000-0003-3765-6401 Daniel A. Perley https://orcid.org/0000-0001-8472-1996 Igor Andreoni https://orcid.org/0000-0002-8977-1498 Eric C. Bellm https://orcid.org/0000-0001-8018-5348 Tracy X. Chen https://orcid.org/0000-0001-9152-6224 Ryan Chornock https://orcid.org/0000-0002-7706-5668 Sofia Covarrubias https://orcid.org/0000-0003-1858-561X Kaustav Das https://orcid.org/0000-0001-8372-997X Christoffer Fremling https://orcid.org/0000-0002-4223-103X

K. R. Hinds https://orcid.org/0000-0002-0129-806X Dan Jarvis https://orcid.org/0009-0004-3067-2227 Mansi M. Kasliwal https://orcid.org/0000-0002-5619-4938 Chang Liu https://orcid.org/0000-0002-7866-4531 Joseph D. Lyman https://orcid.org/0000-0002-3464-0642 Frank J. Masci https://orcid.org/0000-0002-8532-9395 Thomas A. Prince https://orcid.org/0000-0002-8850-3627 Vikram Ravi https://orcid.org/0000-0002-7252-5485 R. Michael Rich https://orcid.org/0000-0003-0427-8387

```
Reed Riddle https://orcid.org/0000-0002-0387-370X
Cassie Sevilla https://orcid.org/0009-0003-2780-704X
Roger Smith https://orcid.org/0000-0001-7062-9726
Jesper Sollerman  https://orcid.org/0000-0003-1546-6615
Jean J. Somalwar https://orcid.org/0000-0001-8426-5732
Gokul P. Srinivasaragavan https://orcid.org/0000-0002-
6428-2700
Jada L. Vail https://orcid.org/0009-0000-4044-8799
Jacob L. Wise https://orcid.org/0000-0003-0733-2916
```

```
Sol Bin Yun https://orcid.org/0009-0000-4440-155X
                              References
Alexander, K. D., Berger, E., Guillochon, J., Zauderer, B. A., &
   Williams, P. K. G. 2016, ApJL, 819, L25
Alexander, K. D., van Velzen, S., Horesh, A., & Zauderer, B. A. 2020, SSRv,
Andalman, Z. L., Liska, M. T. P., Tchekhovskoy, A., Coughlin, E. R., &
  Stone, N. 2022, MNRAS, 510, 1627
Andreoni, I., Coughlin, M. W., Perley, D. A., et al. 2022, Natur, 612, 430
Astropy Collaboration, Price-Whelan, A. M., Lim, P. L., et al. 2022, ApJ,
Astropy Collaboration, Price-Whelan, A. M., Sipőcz, B. M., et al. 2018, AJ,
  156, 123
Astropy Collaboration, Robitaille, T. P., Tollerud, E. J., et al. 2013, A&A,
Bandopadhyay, A., Fancher, J., Athian, A., et al. 2024, ApJL, 961, L2
Barthelmy, S. D., Barbier, L. M., Cummings, J. R., et al. 2005, SSRv, 120, 143
Beck, R., Dobos, L., Budavári, T., Szalay, A. S., & Csabai, I. 2016, MNRAS,
   460, 1371
Bellm, E. C., Kulkarni, S. R., Barlow, T., et al. 2019a, PASP, 131, 068003
Bellm, E. C., Kulkarni, S. R., Graham, M. J., et al. 2019b, PASP, 131, 018002
Beniamini, P., Piran, T., & Matsumoto, T. 2023, MNRAS, 524, 1386
Best, P. N., Kauffmann, G., Heckman, T. M., et al. 2005, MNRAS, 362, 25
Blagorodnova, N., Neill, J. D., Walters, R., et al. 2018, PASP, 130, 035003
Bloom, J. S., Giannios, D., Metzger, B. D., et al. 2011, Sci, 333, 203
Bonnerot, C., Lu, W., & Hopkins, P. F. 2021, MNRAS, 504, 4885
Bonnerot, C., & Stone, N. C. 2021, SSRv, 217, 16
Brown, G. C., Levan, A. J., Stanway, E. R., et al. 2015, MNRAS, 452, 4297
Burrows, D. N., Hill, J. E., Nousek, J. A., et al. 2005, SSRv, 120, 165
Burrows, D. N., Kennea, J. A., Ghisellini, G., et al. 2011, Natur, 476, 421
Cappellari, M. 2017, MNRAS, 466, 798
Cappellari, M., & Emsellem, E. 2004, PASP, 116, 138
Carroll, S. M. 2004, Spacetime and Geometry. An Introduction to General
  Relativity (San Francisco, CA: Addison Wesley)
Cash, W. 1979, ApJ, 228, 939
Cendes, Y., Alexander, K. D., Berger, E., et al. 2021, ApJ, 919, 127
Cenko, S. B., Fox, D. B., Moon, D.-S., et al. 2006, PASP, 118, 1396
Cenko, S. B., Krimm, H. A., Horesh, A., et al. 2012, ApJ, 753, 77
Chambers, K. C., Magnier, E. A., Metcalfe, N., et al. 2016, arXiv:1612.05560
Condon, J. J., Cotton, W. D., & Broderick, J. J. 2002, AJ, 124, 675
Conroy, C., Gunn, J. E., & White, M. 2009, ApJ, 699, 486
Coughlin, E. R., & Nixon, C. J. 2022, MNRAS, 517, L26
Coughlin, E. R., Quataert, E., & Ro, S. 2018, ApJ, 863, 158
Coughlin, M. W., Bloom, J. S., Nir, G., et al. 2023, ApJS, 267, 31
Crumley, P., Lu, W., Santana, R., et al. 2016, MNRAS, 460, 396
Cutri, R. M., Wright, E. L., Conrow, T., et al. 2021, vCat, 2328, 0
De Colle, F., & Lu, W. 2020, NewAR, 89, 101538
Dekany, R., Smith, R. M., Riddle, R., et al. 2020, PASP, 132, 038001
Drout, M. R., Chornock, R., Soderberg, A. M., et al. 2014, ApJ, 794, 23
Duchesne, S. W., Thomson, A. J. M., Pritchard, J., et al. 2023, PASA, 40, e034
Duev, D. A., Mahabal, A., Masci, F. J., et al. 2019, MNRAS, 489, 3582
Dyer, M. J., Ackley, K., Jiménez-Ibarra, F., et al. 2024, Proc. SPIE, 13094,
  130941X
Eftekhari, T., Berger, E., Zauderer, B. A., Margutti, R., & Alexander, K. D.
```

2018, ApJ, 854, 86 Eftekhari, T., Tchekhovskoy, A., Alexander, K. D., et al. 2024, ApJ, 974, 149

Faris, S., Arcavi, I., Makrygianni, L., et al. 2024, ApJ, 969, 104 Foreman-Mackey, D., Hogg, D. W., Lang, D., & Goodman, J. 2013, PASP, 125, 306

Fouka, M., & Ouichaoui, S. 2013, RAA, 13, 680

Fremling, C., Miller, A. A., Sharma, Y., et al. 2020, ApJ, 895, 32 Gafton, E., & Rosswog, S. 2019, MNRAS, 487, 4790

Gehrels, N., Chincarini, G., Giommi, P., et al. 2004, ApJ, 611, 1005

```
Generozov, A., Mimica, P., Metzger, B. D., et al. 2017, MNRAS, 464, 2481
Gezari, S. 2021, ARA&A, 59, 21
Graham, M. J., Kulkarni, S. R., Bellm, E. C., et al. 2019, PASP, 131, 078001
Granot, J., Panaitescu, A., Kumar, P., & Woosley, S. E. 2002, ApJL, 570, L61
Granot, J., & Sari, R. 2002, ApJ, 568, 820
Greene, J. E., Strader, J., & Ho, L. C. 2020, ARA&A, 58, 257
Guillochon, J., McCourt, M., Chen, X., Johnson, M. D., & Berger, E. 2016,
    pJ, 822, 48
Guillochon, J., & Ramirez-Ruiz, E. 2013, ApJ, 767, 25
Guolo, M., Gezari, S., Yao, Y., et al. 2024, ApJ, 966, 160
Hammerstein, E., van Velzen, S., Gezari, S., et al. 2023, ApJ, 942, 9
Hardcastle, M. J., Williams, W. L., Best, P. N., et al. 2019, A&A, 622, A12
Hickox, R. C., Jones, C., Forman, W. R., et al. 2009, ApJ, 696, 891
Hills, J. G. 1975, Natur, 254, 295
Ho, A. Y. Q., Perley, D. A., Beniamini, P., et al. 2020, ApJ, 905, 98
Ho, A. Y. Q., Perley, D. A., Gal-Yam, A., et al. 2023, ApJ, 949, 120
Holoien, T. W. S., Vallely, P. J., Auchettl, K., et al. 2019, ApJ, 883, 111
Hook, I. M., Jørgensen, I., Allington-Smith, J. R., et al. 2004, PASP, 116, 425
Huang, S., Jiang, N., Zhu, J., et al. 2024, ApJL, 964, L22
Huang, X., Davis, S. W., & Jiang, Y.-f. 2023, ApJ, 953, 117
Huang, X., Davis, S. W., & Jiang, Y.-f. 2024, ApJ, 974, 165
IRSA 2022, Zwicky Transient Facility Image Service, IPAC, doi:10.26131/
  IRSA539
Jankovič, T., & Gomboc, A. 2023, ApJ, 946, 25
Jiang, Y.-F., Guillochon, J., & Loeb, A. 2016, ApJ, 830, 125
Johnson, B. D., Leja, J., Conroy, C., & Speagle, J. S. 2021, ApJS, 254, 22
Kaastra, J. S., & Bleeker, J. A. M. 2016, A&A, 587, A151
Kauffmann, G., Heckman, T. M., & Best, P. N. 2008, MNRAS, 384, 953
Kim, Y. L., Rigault, M., Neill, J. D., et al. 2022, PASP, 134, 024505
Komossa, S. 2015, JHEAp, 7, 148
Kormendy, J., & Ho, L. C. 2013, ARA&A, 51, 511
Lacy, J. H., Townes, C. H., & Hollenbach, D. J. 1982, ApJ, 262, 120
Lang, A., Horesh, A., Sfaradi, I., et al. 2024, TNSAN, 205, 1
Leloudas, G., Fraser, M., Stone, N. C., et al. 2016, NatAs, 1, 0002
Levan, A. J., Tanvir, N. R., Cenko, S. B., et al. 2011, Sci, 333, 199
Lodato, G., Franchini, A., Bonnerot, C., & Rossi, E. M. 2015, JHEAp, 7, 158
Mahabal, A., Rebbapragada, U., Walters, R., et al. 2019, PASP, 131, 038002
Mangano, V., Burrows, D. N., Sbarufatti, B., & Cannizzo, J. K. 2016, ApJ,
Masci, F. J., Laher, R. R., Rusholme, B., et al. 2019, PASP, 131, 018003
Masci, F. J., Laher, R. R., Rusholme, B., et al. 2023, arXiv:2305.16279
Matsumoto, T., & Metzger, B. D. 2023, MNRAS, 522, 4028
Matsumoto, T., & Piran, T. 2021, MNRAS, 507, 4196
McMullin, J. P., Waters, B., Schiebel, D., Young, W., & Golap, K. 2007, in
   ASP Conf. Ser. 376, Astronomical Data Analysis Software and Systems
   XVI, ed. R. A. Shaw, F. Hill, & D. J. Bell (San Francisco, CA: ASP), 127
Mimica, P., Giannios, D., Metzger, B. D., & Aloy, M. A. 2015, MNRAS,
   450, 2824
Moffet, A. T. 1975, in Galaxies and the Universe, ed. A. Sandage,
   M. Sandage, & J. Kristian (Chicago, IL: Univ. of Chicago Press), 211
Nicholl, M., Srivastav, S., Fulton, M. D., et al. 2023, ApJL, 954, L28
Nixon, C. J., Coughlin, E. R., & Miles, P. R. 2021, ApJ, 922, 168
Oke, J. B., Cohen, J. G., Carr, M., et al. 1995, PASP, 107, 375
```

Oke, J. B., & Gunn, J. E. 1982, PASP, 94, 586

```
Pasham, D. R., Cenko, S. B., Levan, A. J., et al. 2015, ApJ, 805, 68
Pasham, D. R., Lucchini, M., Laskar, T., et al. 2023, NatAs, 7, 88
Pasham, D. R., Zajaček, M., Nixon, C. J., et al. 2024, Natur, 630, 325
Perley, D. A. 2019, PASP, 131, 084503
Perley, D. A., Fremling, C., Sollerman, J., et al. 2020, ApJ, 904, 35
Perley, R. A., Chandler, C. J., Butler, B. J., & Wrobel, J. M. 2011, ApJL,
  739, L1
Piran, T., Svirski, G., Krolik, J., Cheng, R. M., & Shiokawa, H. 2015, ApJ,
  806, 164
Planck Collaboration, Aghanim, N., Akrami, Y., et al. 2020, A&A, 641, A6
Predehl, P., Andritschke, R., Arefiev, V., et al. 2021, A&A, 647, A1
Prochaska, J. X., Hennawi, J. F., Westfall, K. B., et al. 2020, JOSS, 5, 2308
Pursiainen, M., Childress, M., Smith, M., et al. 2018, MNRAS, 481, 894
Rees, M. J. 1988, Natur, 333, 523
Rigault, M., Neill, J. D., Blagorodnova, N., et al. 2019, A&A, 627, A115
Roberson, M., Fremling, C., & Kasliwal, M. 2022, JOSS, 7, 3612
Roming, P. W. A., Kennedy, T. E., Mason, K. O., et al. 2005, SSRv, 120,
Roth, N., Kasen, D., Guillochon, J., & Ramirez-Ruiz, E. 2016, ApJ, 827, 3
Rybicki, G. B., & Lightman, A. P. 1986, Radiative Processes in Astrophysics
   (Weinheim: Wiley-VCH)
Sabater, J., Best, P. N., Hardcastle, M. J., et al. 2019, A&A, 622, A17
Sari, R. 1998, ApJL, 494, L49
Schawinski, K., Urry, C. M., Simmons, B. D., et al. 2014, MNRAS, 440, 889
Schlafly, E. F., & Finkbeiner, D. P. 2011, ApJ, 737, 103
Sevilla, J., Vail, J. L., Liu, C., et al. 2024, TNSAN, 155, 1
Shimwell, T. W., Hardcastle, M. J., Tasse, C., et al. 2022, A&A, 659, A1
Siebert, M. R., Foley, R. J., Jones, D. O., et al. 2019, MNRAS, 486, 5785
Smith, K. W., Smartt, S. J., Young, D. R., et al. 2020, PASP, 132, 085002
Steele, I. A., Smith, R. J., Rees, P. C., et al. 2004, Proc. SPIE, 5489, 679
Strubbe, L. E., & Quataert, E. 2009, MNRAS, 400, 2070
Sunyaev, R., Arefiev, V., Babyshkin, V., et al. 2021, A&A, 656, A132 Tachibana, Y., & Miller, A. A. 2018, PASP, 130, 128001
Tonry, J. L., Denneau, L., Flewelling, H., et al. 2018a, ApJ, 867, 105
Tonry, J. L., Denneau, L., Heinze, A. N., et al. 2018b, PASP, 130, 064505
Vail, J., Phillips, H., & Pope, J. 2024, TNSTR, 1833, 1
van der Walt, S., Crellin-Quick, A., & Bloom, J. 2019, JOSS, 4, 1247
van Velzen, S., Frail, D. A., Körding, E., & Falcke, H. 2013, A&A, 552, A5
van Velzen, S., Gezari, S., Hammerstein, E., et al. 2021, ApJ, 908, 4
Wang, Y., Wang, T., Jiang, N., et al. 2024, ApJ, 966, 136
Wevers, T., Coughlin, E. R., Pasham, D. R., et al. 2023, ApJL, 942, L33
Wevers, T., Pasham, D. R., van Velzen, S., et al. 2021, ApJ, 912, 151
Williams, P. K. G., Clavel, M., Newton, E., & Ryzhkov, D., 2017 pwkit:
  Astronomical utilities in Python, Astrophysics Source Code Library,
  v1.2.0, ascl: 1704.001
Willingale, R., Starling, R. L. C., Beardmore, A. P., Tanvir, N. R., &
  O'Brien, P. T. 2013, MNRAS, 431, 394
Wiseman, P., Pursiainen, M., Childress, M., et al. 2020, MNRAS, 498, 2575
Yao, Y., Lu, W., Guolo, M., et al. 2022, ApJ, 937, 8
Yao, Y., Lu, W., Harrison, F., et al. 2024, ApJ, 965, 39
Yao, Y., Ravi, V., Gezari, S., et al. 2023, ApJL, 955, L6
Yuan, C., Winter, W., Zhang, B. T., Murase, K., & Zhang, B. 2025, ApJ,
Zauderer, B. A., Berger, E., Soderberg, A. M., et al. 2011, Natur, 476, 425
```